

## Invited Article

# Tungsten oxide films by radio-frequency magnetron sputtering for near-infrared photonics

Hao Chen<sup>a,b</sup>, Alessandro Chiasera<sup>c</sup>, Stefano Varas<sup>c</sup>, Osman Sayginer<sup>c</sup>, Cristina Armellini<sup>c,d</sup>,  
Giorgio Speranza<sup>d</sup>, Raffaella Suriano<sup>e</sup>, Maurizio Ferrari<sup>c</sup>, Silvia Maria Pietralunga<sup>b,f,\*</sup>

<sup>a</sup> Dipartimento di Fisica, Politecnico di Milano, Piazza L. da Vinci, 32, 20133, Milano, Italy

<sup>b</sup> CNST@Polimi, Istituto Italiano di Tecnologia (IIT), Via Giovanni Pascoli 70/3, Milano, Italy

<sup>c</sup> Institute for Photonics and Nanotechnologies (IFN)—National Research Council (CNR) CSMFO Lab. and Fondazione Bruno Kessler (FBK) Photonics Unit, Via alla Cascata 56/C, 38123, Trento, Italy

<sup>d</sup> Fondazione Bruno Kessler (FBK)—Centro Materiali e Microsistemi (CMM), Via alla Cascata 56/C, 38123, Trento, Italy

<sup>e</sup> Department of Chemistry, Materials and Chemical Engineering “Giulio Natta”, Politecnico di Milano, Piazza L. da Vinci, 32, 20133, Milano, Italy

<sup>f</sup> Institute for Photonics and Nanotechnologies (IFN)—National Research Council (CNR), Piazza L. da Vinci, 32, 20133, Milano, Italy



## ARTICLE INFO

## Keywords:

Tungsten oxide  
NIR transparency  
Optical anisotropy  
Wide-bandgap semiconductors  
Photonic bandgap materials  
Radio-frequency sputtering

## ABSTRACT

Tungsten oxide  $\text{WO}_{3-x}$  is a transition metal oxide and a wide bandgap semiconductor, with a wide range of possible optical and photonic applications. In dependence on the fabrication techniques different stoichiometric ratios ( $x$ ) and crystalline phases are obtained, which end up with an overall polymorph and extremely versatile material, characterized by tailorable dielectric properties. In particular,  $\text{WO}_{3-x}$  thin film deposition by Radio-Frequency (RF) sputtering techniques provides a precise control of thickness, composition and nanostructure. In this work we introduce and discuss a specific process of deposition, that is magnetron RF-sputtering as a suitable way to grow  $\text{WO}_{3-x}$  thin films with selected properties. Possibility of integrating  $\text{WO}_{3-x}$  thin film on to one-dimensional (1D) photonic crystal structures is also explored. Films are transparent in the near and short-wavelength infrared optical spectral range. Their quality is assessed by morphological, structural and compositional characterizations. Dielectric properties are characterized by optical spectroscopy and ellipsometry, the latter also evaluates the degree of optical anisotropy of thin films in their crystalline phase. An 1D photonics bandgap structure is designed, formed by a  $\text{SiO}_2$ - $\text{TiO}_2$  multilayer and capped with a 450 nm-thick transparent  $\text{WO}_{3-x}$  film, so that surface confinement and local enhancement of the optical field at 1416 nm in the topmost  $\text{WO}_{3-x}$  layer is obtained.

## 1. Introduction

The research interest for tungsten oxide ( $\text{WO}_3$ ) as a wide-bandgap semiconductor has increased over the latest decades, prompted by its extraordinarily broad range of applications [1].  $\text{WO}_3$  is a polymorph material that stabilizes several different crystalline phases at atmospheric pressure according to temperature [2–4]. Also in presence of oxygen deficiency, sub-stoichiometric  $\text{WO}_{3-x}$  ( $0.05 < x < 0.375$ ) can form different stable crystalline phases (*Magnéli phases*) [5]. Broadly speaking, dielectric and optical properties of  $\text{WO}_{3-x}$  are strongly affected by the value of the compositional ratio  $x$  [6]. The stoichiometry, as well as the presence of impurities, also determine the  $n$ -type or  $p$ -type electrical character of tungsten oxide as a semiconductor [1,5,7]. Generally

in oxygen-deficient  $\text{WO}_{3-x}$  phases,  $n$ -type electrical conductivity is preferably expressed [6]. Sub-stoichiometric phases with  $x > 0.1$  may even change from being semiconducting to metal-like [5,8]. Just to list some among the main applications of  $\text{WO}_{3-x}$ , crystalline nanorods [9] and nanowires behave as electrical field emitters [10], compact and smooth optical thin films are used in smart windows [11–16] and UV optical detectors [17–19] thanks to their chromogenic qualities, nano-porous films are exploited in sensors [20–25] and photo-electro-catalytic devices [26–29]. Full-optical chemical sensors have also been proposed, by optically read-out of chemically induced variations of dielectric response in thin films of  $\text{WO}_{3-x}$  [30]. Throughout this work, we will generally refer to  $\text{WO}_{3-x}$  ( $0 \leq x < 1$ ) as tungsten oxide, therefore comprising both its stoichiometric and sub-stoichiometric

\* Corresponding author. Institute for Photonics and Nanotechnologies (IFN)—National Research Council (CNR), Piazza L. da Vinci, 32, 20133, Milano, Italy.  
E-mail address: [silvia.pietralunga@ifn.cnr.it](mailto:silvia.pietralunga@ifn.cnr.it) (S.M. Pietralunga).

<https://doi.org/10.1016/j.omx.2021.100093>

Received 5 August 2021; Received in revised form 19 September 2021; Accepted 20 September 2021

Available online 7 October 2021

2590-1478/© 2021 The Author(s). Published by Elsevier B.V. This is an open access article under the CC BY license (<http://creativecommons.org/licenses/by/4.0/>).

forms.

Among the different methods of synthesis for tungsten oxide films [31], Radio-Frequency (RF) sputtering has established itself as a versatile one, with the advantage of providing fabrication processes upgradable to the industrial scale. Through a precise control of growth and by tuning a whole set of deposition parameters, this technique may provide not only porous films for sensing [23–25] and advanced photo-electro-catalytic devices [26–28], but also smooth and compact layers of good optical quality [12–14,32–36]. In this work we show that non-reactive magnetron RF-sputtering in Ar atmosphere at room temperature (RT), followed by post-growth thermal annealing in dry air, is a suitable technique to fabricate compact and smooth  $WO_{3-x}$  optical thin films. Annealing in air provides an effective and direct means of adjusting the compositional ratio, thus manipulating the structure and dielectric properties of the material, whilst keeping the optical grade. We have correlated deposition and annealing of the films to a comprehensive characterization of their morphology, structure, chemical configuration and dielectric properties. In their *as-deposited* form, RF-sputtered thin films are sub-stoichiometric and optically opaque in the visible and near-IR range. An 8-h annealing step at 300 °C considerably increases the transparency of the films and widens the optical bandgap, suggesting that a nearly fully oxidized stoichiometry can be reached while preserving an amorphous structure. By annealing at 400 °C films crystallize in addition to be more transparent. We evaluate and discuss the evolution in composition, structure and dielectric properties induced by thermal annealing, from the quasi-metallic character of *as-deposited* samples to their dielectric behavior after annealing. In particular, by analysing the spectral dispersion of the complex dielectric function with spectroscopic ellipsometry, we show that annealed films are quite transparent in the near infrared (NIR) and short-wave infrared (SWIR) optical range. And we also evaluate the intrinsic birefringence of anisotropic crystalline phase. Finally, in exploitation of  $WO_{3-x}$  thin layers as optical chemical sensors, by optical wave numerical simulation we analyse the design conditions of integrating a  $WO_{3-x}$  layer on to the top of an 1D Photonic bandgap (1D-PBG) structure. It is known that optical field can be predominantly confined in the topmost layers of suitably designed 1D-PBG, thus enhancing the interaction with environment [37]. In present work, starting from the results provided by the spectroscopic characterization of dielectric function in  $WO_{3-x}$  films, we have designed a resonant structure capable to effectively confine incident light in  $WO_{3-x}$  layer at surface.

## 2. Materials and methods

### 2.1. Film preparation

Tungsten oxide thin films were deposited by non-reactive RF magnetron sputtering onto three different substrates, namely *p*-type doped Silicon wafers (100)-oriented, fused silica slides ( $SiO_2$ ) and Indium-Tin-Oxide (ITO)-coated borosilicate glass slides (sheet resistance: 8–12  $\Omega$ /square). Before deposition, in order to remove adsorbed contaminants, substrates were cleaned first by rinsing them in ethanol and then by heating them at 120 °C for 30 min in a pre-chamber (at pressure below  $1 \times 10^{-5}$  mbar). For silicon wafer, a very thin layer of native oxide can exist on the surface due to the exposure to the atmosphere and was not removed in this experiment. Cleaned substrates were transferred into the deposition chamber and placed aside on the same holder, to proceed with the growth of nominally identical film samples. The base pressure in chamber was set at  $2.5 \times 10^{-7}$  mbar and the working pressure was stabilized at  $5.4 \times 10^{-3}$  mbar by inletting 99.99% pure argon (Ar) gas as a media for plasma discharge. The operating sputtering power was set to be 80 W at RF = 13.56 MHz. A stoichiometric  $WO_3$  rectangular ( $2 \times 5.625$  inch) target (SEMATRADE, purity of 99.95%) was placed at a distance of 250 mm from the substrates. The surface of the target was also cleaned by pre-sputtering for 10 min before to start deposition, in the meantime keeping the substrates sheltered.

The target was kept at a constant temperature of 17 °C by a cooling system (SMC Chiller mod. HRS024-AF-20-T). The temperature of substrates was stabilized at room temperature by thermal dissipation through the copper sample holder [38,39]. After deposition, post-growth annealing steps in dry air were carried out for 8 h using a conventional tubular oven (Carbolite mod. CTF). The thermal treatment time had been preliminary optimized [39]. Two annealing temperatures were chosen, namely 300 °C and 400 °C, which are respectively below and above the reported threshold for  $WO_3$  crystallization [40]. Two reference values for film thickness were obtained, respectively around 200 nm and 60 nm, by changing the deposition time at the same nominal growth conditions. In this way, six samples were finally prepared, respectively labelled as S1, S2 and S3 (thicker set) and S4, S5 and S6 (thinner set). Samples S1 and S4 were kept *as-deposited* and not annealed, while samples S2 and S5 were annealed at 300 °C, and samples S3 and S6 were annealed at 400 °C. Each one of the samples was fabricated on all of the three substrates, to provide suitable environments for different characterizations.

### 2.2. Methods of characterization

The eligibility of the RF-sputtering/annealing as a fabrication process for optical grade  $WO_{3-x}$  films with selected dielectric properties was assessed by performing comparative and correlated characterizations of the structural, morphological, physio-chemical, and dielectric properties of samples, both *as-deposited* and thermally annealed. Film thickness was evaluated by cross-sectional imaging in High-Resolution Scanning Electron Microscope (HRES-SEM, Tescan MIRA3) and confirmed by step profilometry (VEECO Dektak 150). Atomic force microscopy (AFM) has been applied to characterize the morphology and roughness at the surface of films, by using an NSCRIPTOR DPN system, driven by SPM Cockpit software (NanoInk., Skokie, IL) in tapping mode at ambient temperature and humidity. Measurements were obtained using commercially available silicon ACT tips (AppNano - Santa Clara, CA) with a nominal spring constant of 40 N/m (nominal value of tip radius = 6 nm). The AFM 3D maps were obtained at 0.2 Hz of scan frequency and were evaluated by using NanoRule + <sup>TM</sup> AFM software (Pacific Nanotechnology - USA). The arithmetic mean roughness ( $R_a$ ) (Eqn 1) which represents the arithmetic mean of the measured ordinates  $Z(x, y)$  within the analysed area, was calculated according to following equation:

$$R_a = \frac{\sum_{i=1}^N |Z_i - \bar{Z}|}{N} \quad (1)$$

where  $\bar{Z}$  is the average of measured heights, as follows (Eqn 2):

$$\bar{Z} = \frac{\sum_{i=1}^N Z_i}{N} \quad (2)$$

And  $N$  is the number of points included in the analysed surface.

The crystallinity was assessed by X-Ray Diffraction (XRD) using a X'Pert Pro Panalytical diffractometer, equipped with graphite-monochromatized  $Cu K\alpha_1$  radiation at a wavelength of 1.54060 Å. Samples deposited on (100) Si substrates were characterized at grazing incidence (5°), in order to maximize the contribution from  $WO_{3-x}$  thin films and to minimize the effect from substrate. The patterns were acquired over the angle range  $2\theta = 20 \sim 100^\circ$  with a step size of 0.05° in Bragg-Brentano geometry and the time for each step was 5s. The operating voltage and current were 40kV and 35mA, respectively. The composition of the samples was evaluated using X-ray photoelectron spectroscopy (XPS), with particular attention to the oxidation state of W. XPS spectra were acquired using an Axis DLD Ultra instrument (Kratos – Manchester UK). For each sample, the analysis was composed by a wide spectrum on Binding Energy (BE) range 1250 to –5 eV using a 160eV pass energy. For each of W, O and C elements, high resolution core line spectra were collected by setting the analyser pass energy at 20eV with

an energy step of 0.05 eV. Charge compensation was applied when necessary, tuning the compensation conditions to maximize the peak intensity while minimizing its Full-Width Half-Maximum (FWHM). The XPS spectral data reduction was performed using a home-made software based on the R platform [41]. Spectra were aligned on the BE scale taking the  $W_{4f}$  main peak at 35.8 V as a reference. Care was taken in selecting appropriate background subtraction and Gaussian components for peak fitting.

The optical absorbance of films in the range from ultraviolet (UV) to near infrared (NIR) was characterized by Optical UV–Vis–NIR Spectrometry (Cary Varian 5000) on samples deposited onto  $SiO_2$ . By applying Tauc method analysis to the absorbance data, the amplitude of optical bandgap has been estimated [42]. Details of the procedure are reported in Appendix A. Characterizations of linear optical properties were complemented by measuring the dispersion of complex dielectric function of  $WO_{3-x}$  films in the  $350 \text{ nm} < \lambda < 1700 \text{ nm}$  spectral range by Variable Angle Spectroscopic Ellipsometry (VASE) (J.A. Woollam Co., Inc.) [43]. The principle of operation of VASE is briefly summarized in Appendix B. Values of complex dielectric functions  $\tilde{\epsilon}(\lambda)$  are obtained by performing a fitting of experimentally measured values of the ellipsometric functions  $\Psi(\theta, \lambda)$  and  $\Delta(\theta, \lambda)$  to a reference dielectric model (see Appendix B for further details). The reference model includes parametric expressions for complex dielectric functions and thickness of all the layers, and is refined by fitting for morphological and structural information, such as porosity, surface roughness, homogeneity, and anisotropy. Measurements were carried out at 10-nm-steps and at three angles of incidence  $65^\circ$ ,  $70^\circ$  and  $75^\circ$ . The data analysis and fitting was performed using commercially available WVASE32 software and the Levenberg-Marquardt regression algorithm was used for minimizing the mean-squared error (MSE) [44].

### 2.3. Design of photonic structure for optical field enhancement in $WO_{3-x}$ layer

Optical localization can be obtained by depositing  $WO_{3-x}$  films on top of photonic resonant structures, such as 1D-PBG and Bragg reflectors [37]. To this aim, a multilayer structure has been conceived, as formed by the sequence of alternated  $SiO_2$  and  $TiO_2$  layers and capped with  $WO_{3-x}$ . The structure has been designed to minimize optical transmission and to maximize reflection over the range from 890 nm to 1450 nm, and so that bandgap edges occur in the NIR. Firstly, the  $SiO_2/TiO_2$  multilayer was designed. The thickness of the  $SiO_2$  layer was determined using the quarter-wave approach [45] and the thickness of the  $TiO_2$  layer was chosen using a set of transfer matrix (TM) calculations for a well-tuned spectrum [46,47]. The TM calculations were performed at normal optical incidence and by using wavelength-dependent refractive index values  $n(\lambda)$  for  $SiO_2$  and  $TiO_2$  [48,49]. Then, the distribution of optical field intensity in  $WO_{3-x}$  topmost layer was calculated using a 3D finite element model (FEM) by COMSOL Multiphysics®. More in detail, a square cell of  $1 \mu\text{m}$  in size was considered and frequency domain

analysis consisting of periodic boundary condition (Floquet periodicity) with zero-incidence angle wave excitation at the top layer was adopted. In order to determine the ideal thickness of  $WO_{3-x}$  layer, a parametric thickness sweep study was performed from 100 nm to 500 nm with an increment size of 10 nm and by evaluating the total electric field norm at band edge wavelengths (from 1400 nm to 1700 nm with 10 nm-steps). The optical dispersion of  $WO_{3-x}$  film in the NIR was modelled by using the refractive index values for sample S6 as evaluated in present work.

## 3. Results and discussion

### 3.1. Morphology and structure

The HRES-SEM cross-sectional images of samples S1 (*as-deposited*), S2 (annealed at  $300^\circ\text{C}$ ) and S3 (annealed at  $400^\circ\text{C}$ ) grown on Si substrate are shown in Fig. 1 and show the compactness and smoothness of RF-sputtered  $WO_{3-x}$  thin films. In the case of S3, the visible contrast pattern is an indication of some degree of structurization in the film thickness. Mean values for thickness  $d$  were evaluated by averaging multiple measurements across the cleaved sections, and results are reported in Table 1. Thickness was substantially confirmed by step profilometry within measurement accuracy.

Surface morphology and roughness were analysed by AFM at different spots on the samples grown on ITO-coated glass. Fig. 2 shows representative 2D AFM maps, scanned over  $4 \mu\text{m}^2$  area for thicker and thinner sets of samples. In thicker films S1 and S2, round-shaped nanoparticles with a diameter ranging from 150 to 200 nm can be noticed. The dimension of nanoparticles seems to decrease in sample S3, where their presence is sometimes unrecognizable. Regarding the thinner set, the topography of three zones looks somewhat equivalent, even though in case of S5 the formation of a different patterning can be inferred. Moreover, AFM topographical images of sample S4 reveals the presence of clusters of ellipsoidal nanoparticles with a shorter width of 50–100 nm, together with nanoparticles having a similar shape but higher dimensions of 180–250 nm. After annealing, 50–250 nm-sized nanoparticles with a more rounded shape can be observed in S5 and S6 samples. When compared with sample S4, S5 (annealed at  $300^\circ\text{C}$ ) shows the presence of larger valley areas between the particles. The analysis software provides very low arithmetic mean roughness values  $R_a$  of respectively 1.83 nm (S1), 1.82 nm (S2), 2.47 nm (S3), 1.59 nm (S4), 1.80 nm (S5) and 1.97 nm (S6) and corresponding peak-to-peak roughness average values of 17.95 nm (S1), 17.33 nm (S2), 26.67 nm (S3), 16.02 nm (S4), 18.40 nm (S5) and 19.05 (S6). The variations in  $R_a$  correlated with the annealing, and its slight increase at  $400^\circ\text{C}$ , are at the atomic scale and their significance might be considered as questionable in the present context. However,  $R_a$  values measured by AFM for samples annealed at  $400^\circ\text{C}$  are found to be higher than those of samples annealed at  $300^\circ\text{C}$  and *as-deposited* films, with particular regard to S3 when compared to S1 and S2. Results are listed in Table 1. Values of  $R_a$  roughly scale with film thickness and are higher for the thicker set, as

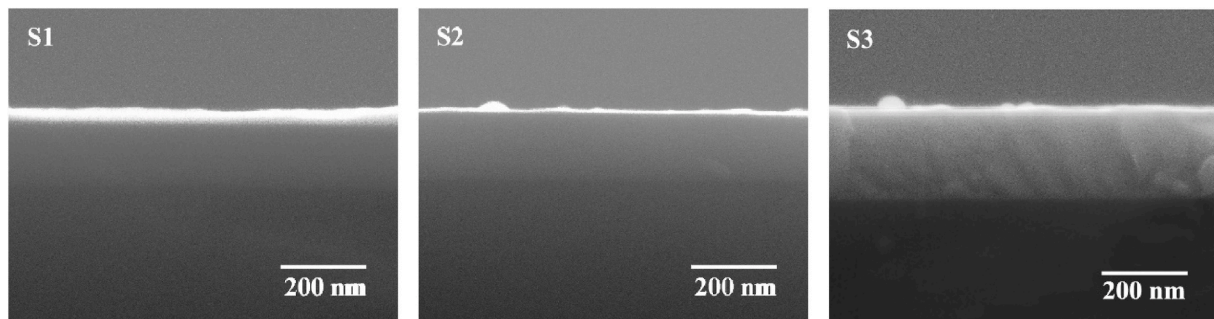
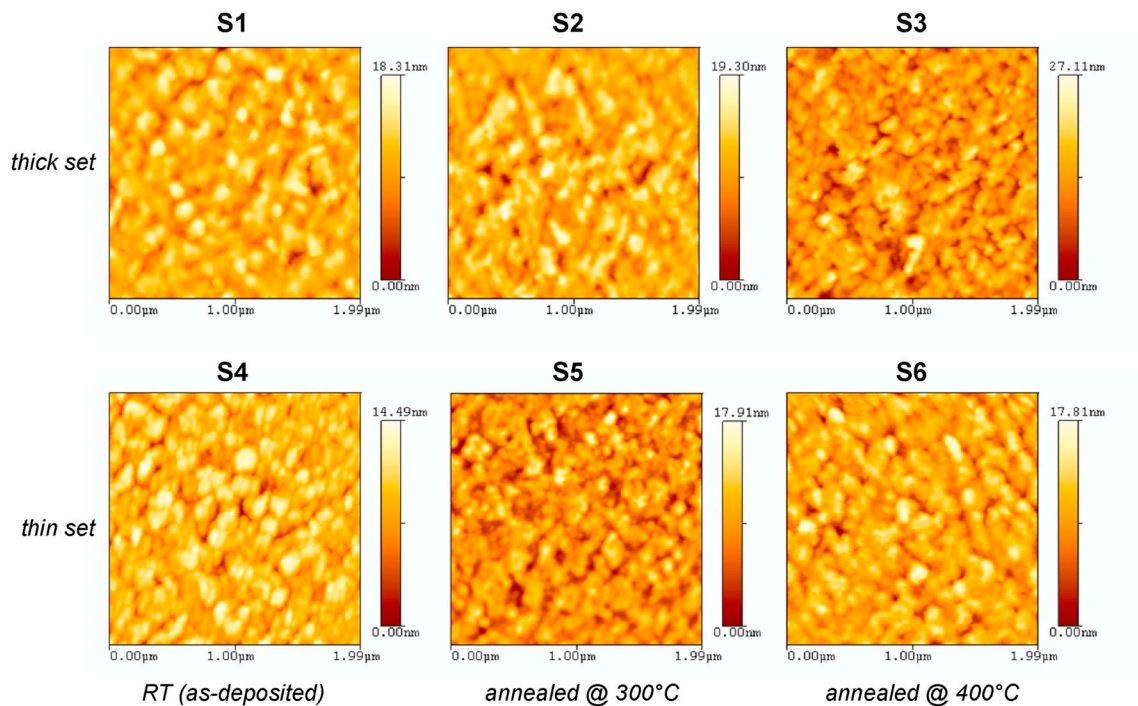


Fig. 1. Cross-Sectional SEM images of  $WO_{3-x}$  thin films deposited through RF sputtering. For morphological description of S1 and S2 also refer to Ref. [50]. (no colour printing required).

**Table 1**  
Morphological, structural, optical, and electrical parameters for  $\text{WO}_{3-x}$  film samples.

Sample	S1	S2	S3	S4	S5	S6
Annealing ( $^{\circ}\text{C}$ )	No	300	400	No	300	400
Thickness (nm)	$162 \pm 5$	$159 \pm 5$	$202 \pm 5$	$43 \pm 5$	$58 \pm 5$	$63 \pm 5$
Symmetry	amorphous	amorphous	monoclinic	Amorphous	amorphous	monoclinic
$R_a$ (nm) AFM	1.83	1.82	2.47	1.59	1.80	1.97
$E_g$ (eV)	2.57	2.84	2.96	2.49	3.05	3.15
$n$ @550 nm	–	–	–	2.37	2.06	2.18
$\kappa$ @550 nm	–	–	–	0.82	$1.97\text{E-}5$	$2.51\text{E-}3$
$n$ @1500 nm	–	–	–	2.89	1.99	2.06
$\kappa$ @1500 nm	–	–	–	0.44	$4.00\text{E-}9$	$3.01\text{E-}5$



**Fig. 2.** Matrix taxonomy of AFM topographic 2D images of samples. First and second row correspond respectively to thicker set {S1, S2, S3} and thinner set {S4, S5, S6}. The type of thermal treatment is specified at the bottom of selected columns. (no colour printing required). (For interpretation of the references to colour in this figure legend, the reader is referred to the Web version of this article.)

analysed both by AFM and profilometry. As a whole, the very small  $R_a$  values are an indication of extremely smooth layers quite fit for those optical applications that involves the propagation of the phase front and coherent processing of field amplitude.

Structural characterization by XRD was performed on films grown on Si (100) substrates. The XRD patterns for *as-deposited* and annealed samples are reported in Fig. 3. A residual broad hump from the scattering of the Si substrate (100) is visible at about  $70^{\circ}$  in all traces. In case of as-grown S1 and S4, the broad peak centred at about  $2\theta = 24^{\circ}$  indicates the typical lack of long-range ordering of an amorphous structure. In samples treated at  $300^{\circ}\text{C}$  (S2 and S5) peak narrowing is negligible. This is an indication that, as expected, annealing up to  $300^{\circ}\text{C}$  does not provide enough energy for nucleation and growth of  $\text{WO}_{3-x}$  crystallites. Instead, samples S3 and S6, which are thermally treated at  $400^{\circ}\text{C}$ , are polycrystalline. The dominance of the (002) peak at about  $2\theta = 23.2^{\circ}$  in sample S6 suggests that the texture of  $\text{WO}_{3-x}$  thin film is a monoclinic phase, space group P21/n, oriented along the c-axis perpendicular to the surface of substrate (JCPDS card 72-1465). In the case of thicker sample S3 the peaks at about  $2\theta = 23.2^{\circ}$  (002),  $23.6^{\circ}$  (020) and  $24.4^{\circ}$  (200) confirm the coexistence of several crystalline orientations of monoclinic stoichiometric  $\text{WO}_3$ . The effects of annealing in air on tungsten oxide films and their crystallization in different phases

according to temperature and substrate have been studied [2]. Though  $\text{WO}_3$  is expected to crystallize as orthorhombic phase at  $400^{\circ}\text{C}$ , transformation into the more stable monoclinic phase may occur while cooling the thin films down to room temperature. Or, the limited thickness of deposited films may favour ordered monoclinic arrangements. Actually, at normal conditions crystalline  $\text{WO}_3$  thin films on substrates are generally reported as monoclinic [2,51,52]. Regarding the difference in peaks between S3 and S6, despite equivalent temperature and duration of the annealing process, different film thicknesses may induce different kinetics that affect the orientational homogeneity of the crystallites. By applying Scherrer formula [53] to the most intense peaks in samples S3 and S6, crystallite size was roughly estimated and minimum average dimension was evaluated at 33 nm and 28 nm, respectively.

The effect of thermal annealing on films is documented by XPS results as shown in Fig. 4. Tungsten core line is plotted in Fig. 4a. The spectrum is formed by two main features that represent the  $W_{4f}$  spin orbit components. An example of peak fitting performed on sample S1 is shown in the inset. Line shape fitting is composed by two main peaks falling at 35.8 eV and 37.9 eV [54]. This doublet is associated to the  $4f_{7/2}$  and  $4f_{5/2}$  spin orbit components of  $W^{6+}$  deriving from  $\text{WO}_3$ . The W core-line also shows a second pair of components located at lower BE,

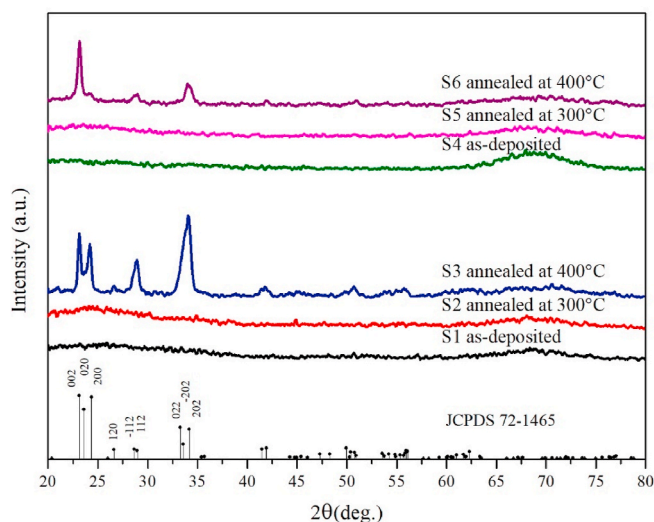


**Fig. 3.** XRD patterns of the RF-sputtered  $\text{WO}_{3-x}$  films with and without post-annealing treatments. Peak position and planes indices are shown at the bottom, based on JCPDS card 72-1465. (no colour printing required). (For interpretation of the references to colour in this figure legend, the reader is referred to the Web version of this article.)

respectively at 34.6 eV and 36.97 eV, that can be assigned to the  $4f_{7/2}$  and  $4f_{5/2}$  of  $\text{W}^{+(6-x)}$  ions deriving from sub-stoichiometric  $\text{WO}_{3-x}$ , thus mirroring the presence of oxygen vacancies [55]. These minor components describe the spectral power in the region between the two main peaks and the tail at low BE. These features, which are visible in the film deposited at RT, disappear in annealed samples as the annealing temperature increases. Following the interpretation of W core line, the effect of temperature in annealing is a progressive crystallization and oxidation process of the initially amorphous tungsten oxide phase into a more stoichiometric structure [56,57], leading to the aforementioned loss of spectral power in the indicated regions. The main effect of the annealing temperature on the  $\text{W}_{4f}$  occurs in passing from RT to 300 °C, while a further increasing of temperature seems not to induce relevant changes. There is a broad literature describing the variations of oxygen vacancy density upon annealing [56,58,59]. In this respect, it is important to observe that opposite effects may be obtained, depending on the atmosphere used for the thermal treatments. Annealing in inert atmosphere or vacuum induces an increase of oxygen vacancy concentration,

due to desorption of oxygen induced by the thermal treatment [58,60,61]. On the contrary, a reduction of oxygen vacancies occurs upon annealing in air or in oxygen-rich atmosphere over the thermal range from RT to 300–350 °C [62], as it is likely to occur also in our case and which is compatible with an increase in stoichiometry of  $\text{WO}_{3-x}$ . Fig. 4b shows the changes in the  $\text{O}_{1s}$  spectral behavior. By increasing the annealing temperature from RT to 300 °C and to 400 °C, the  $\text{O}_{1s}$  tail at high BE progressively decreases. The peak fitting performed using four Gaussian components is reported in the inset. The lower fitting component at BE ~530.7 eV is assigned to  $\text{O}^{2-}$  in the  $\text{WO}_3$ . The component falling at 531.2 eV is assigned to  $\text{O}^{2-}$  ions issued by oxygen-deficient regions associated with vacancies [54,63]. However, the same BE can be assigned also to tungsten hydroxide present at sample surface when exposed to air [64,65]. The third component at BE ~532.5 eV can be assigned to oxygen that is bonded to carbon, and the fourth component at BE ~533 eV is from oxygen that derives from adsorbed water. Table 2 summarizes the concentrations of chemical species estimated for samples S1, S2, S3. In particular, the relative contribution of stoichiometric and sub-stoichiometric oxidized tungsten phases to the W content has been evaluated and reported. The evidence of sub-stoichiometric phases implies that the stoichiometry of *as-deposited* films has been somehow decreased although they were deposited starting from the stoichiometric  $\text{WO}_3$  target. This might be due to the fact that, during the deposition process, the oxygen atoms (the mass of which is less) are more gravely scattered to random directions in the chamber as they travel through the plasma, than the peer tungsten atoms (the mass of which is greater) [34]. Randomly scattered atoms are either terminated on the inner wall of chamber or pumped away from the deposition chamber, resulting in a loss of oxygen percentage in the final films. As shown in Table 2, the relative percentage of sub-stoichiometric  $\text{WO}_{3-x}$  with respect to stoichiometric  $\text{WO}_3$  is decreased in crystallized S3 sample, though it is not fully eliminated. The fact that sub-stoichiometric  $\text{WO}_{3-x}$  phases are not seen in the XRD

**Table 2**

Abundances of chemical species found in the deposited films. The relative contribution of stoichiometric  $\text{WO}_3$  and sub-stoichiometric  $\text{WO}_{3-x}$  to the percentage of W content is indicated in *italic*.

Sample	$\text{WO}_3$ (%)	$\text{WO}_{3-x}$ (%)	W (%)	O (%)	C%
S1	<i>15.0</i>	<i>1.7</i>	16.7	54.1	29.1
S2	<i>16.4</i>	<i>1.9</i>	18.3	57.6	24.1
S3	<i>17.0</i>	<i>1.5</i>	18.6	57.4	24.1

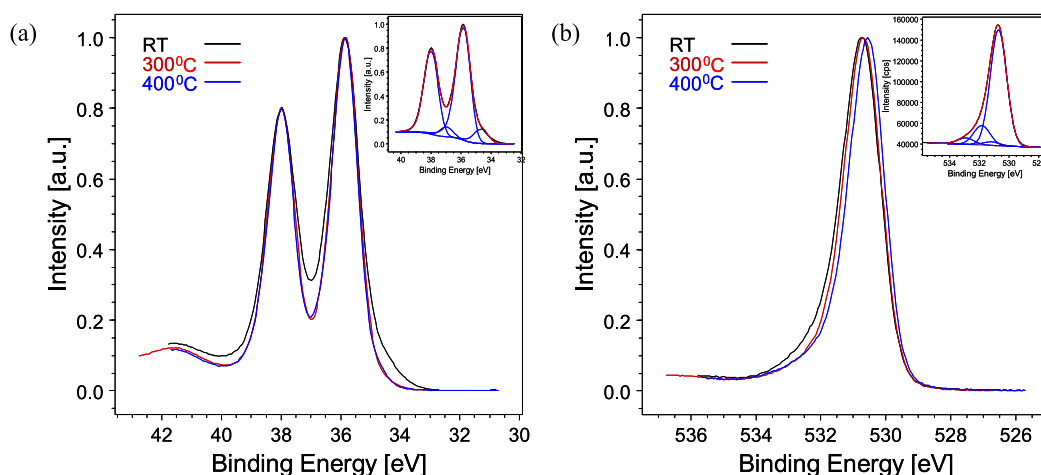


**Fig. 4.** Change of the  $\text{W}_{4f}$  (a) and  $\text{O}_{1s}$  (b) core line spectra as a function of the annealing temperature. The inset shows an example of peak fitting performed on sample S1 deposited at RT. (colour printing required). (For interpretation of the references to colour in this figure legend, the reader is referred to the Web version of this article.)

analysis might be due to the confinement of these sub-stoichiometric phases to the film surface and beyond the XRD detection limit. The presence of carbon at film surface comes from unavoidable contamination when exposed to the ambient air. Instead, the presence of elemental oxygen may come both from oxidized tungsten and from adsorbed moisture.

Previous studies of tungsten oxide nanoarrays on the effect of annealing in air and in vacuum, show that annealing in air causes a reduction of the XPS hydroxylated component of tungsten oxide while annealing in vacuum causes an increase of tungsten sub-oxide components [66]. The former case (i.e., annealing in air) supports that, the annealing in present study causes a removal of OH groups. We have shown that the removal of OH groups at 300 °C combines with an increase in electrical conductivity [50], because OH groups may fill the oxygen vacancies, thus influencing the electrical properties of the material. Desorption of hydroxyl groups renders oxygen vacancies available, thus increasing the number of charge carriers. This tendency is reversed by further increasing the annealing temperature to 400 °C, in corresponding to the transition from amorphous to an orthorhombic crystalline structure [56,57]. In particular in Ref. [57] authors estimated a formation energy respectively of 5.47 eV and 4.88 eV in case of vacancy-defected and relaxed orthorhombic crystalline structures. As it appears from calculations, the elimination of oxygen vacancies with relaxation into a more ordered crystalline structure leads to a lowering of the system energy. Therefore, annealing in air at 400 °C provides sufficient energy to allow the disordered-to-crystalline transition with elimination of vacancy defects. Results are in agreement also with [67] where an increase of the optical gap is obtained by annealing amorphous tungsten oxide films in oxygen atmosphere, which is associated to crystallization and elimination of vacancy-related defects. This interpretation agrees also with the XRD analysis where the onset of WO<sub>3</sub> crystallization is barely visible at 300 °C in the range  $2\theta = 20\text{--}40^\circ$  and becomes evident at 400 °C, mirroring the presence of well-formed WO<sub>3</sub> crystallites.

### 3.2. Optical absorption spectroscopy and bandgap evaluation

*As-deposited* WO<sub>3-x</sub> films look opaque in daylight and turn into transparent by thermal annealing. Fig. 5 compares the absorbance spectra (A) of films deposited onto fused silica substrates in the UV-VIS-NIR range by logarithmic ratio of the detected signal  $I_{out}(\lambda)$  and the input optical intensity  $I_{in}(\lambda)$  as:  $A(\lambda) = -\log_{10} \frac{I_{out}(\lambda)}{I_{in}(\lambda)}$ . Evidently, thicker films lead to overall stronger absorbance than thinner films though fabricated under nominally identical conditions. The threshold for strong absorption at around 350 nm is a contribution from interband optically allowed transitions between electronic levels at top of the valence band (formed by O<sub>2p</sub> orbitals) and at the bottom of the conduction band (formed by

W<sub>5d</sub> orbitals). *As-deposited* films are more absorptive than the annealed ones, and transparency increases with annealing temperature. Oscillations, evident in case of more transparent films, are interference effects from reflections with the substrate. We remark that, unlike what is reported elsewhere for sub-stoichiometric WO<sub>3-x</sub> [68], we see no experimental evidence of a strong increase of absorbance in the NIR range. Strong NIR absorption is justified either in terms of optical excitation of electrons from donor states into the conduction band, or from intraband excitation of free carriers [68]. Thus, neither effect seems to predominantly affect absorption in the present case.

Values of optical bandgap ( $E_g$ ) for the films were derived from absorbance spectra by Tauc plot method [69]. According to Davis and Mott theory [70], close to the bandgap the energy dispersion of absorption in semiconductors follows a power law:

$$(\alpha h\nu)^{1/\beta} = B(h\nu - E_g) \quad (3)$$

where  $\alpha$  is the absorption coefficient ( $\alpha = 2.303A/d$ ),  $h\nu$  is the photon energy,  $E_g$  is the bandgap, and  $B$  is a structural constant that represents the slope of the linear portion of the curve. The exponent  $\beta$  takes the values  $\beta = 1/2$  and  $\beta = 2$ , respectively, to model direct and indirect allowed optical transitions at bandgap. By performing a regression fitting of the linear region of the curve and by extrapolating it to zero absorption,  $E_g$  value is given by the intersection with the energy axis. The direct or indirect nature of bandgap in tungsten oxide has been an object of debate [6,57,71–73]. In present study we discriminate between the two options by comparing both approaches to experimental data. The linear fitting of Tauc plots by assuming direct interband optical transitions ( $\beta = 1/2$ ) issues  $E_g \sim 3.84 \text{ eV} - 4.12 \text{ eV}$  (see Figure A1 in Appendix A). Such values for  $E_g$ , besides exceeding the ones commonly reported for WO<sub>3</sub> and WO<sub>3-x</sub> [73–75], would correspond to absorption edges located in the UV. As such conveys that all of the films should be transparent in the visible range, which is inconsistent with the experimental evidence that *as-deposited* films are opaque under visible light. Also, by admitting direct transitions, a narrowing of optical bandgap with annealing would occur, which should lead to an increase in absorbance, again at odds with experimental results. By contrast, if indirect transitions are assumed ( $\beta = 2$ ), a linear fitting issues values in the range  $E_g \sim 2.56 \text{ eV} - 3.15 \text{ eV}$  that increases with annealing temperature, as reported in Fig. 6 and Table 1. Such values are in substantial agreement with available results for WO<sub>3-x</sub> films grown by sputtering techniques [6, 76], and also properly account for the increased transparency of the annealed samples. The widening of optical bandgap with annealing temperature is likely to correspond to stronger oxidation at higher temperatures, in agreement with XRD and XPS results. The speed and efficiency of oxidation effect depends on the thermal kinetic energy of external oxygen atoms, which well explains why the higher annealing

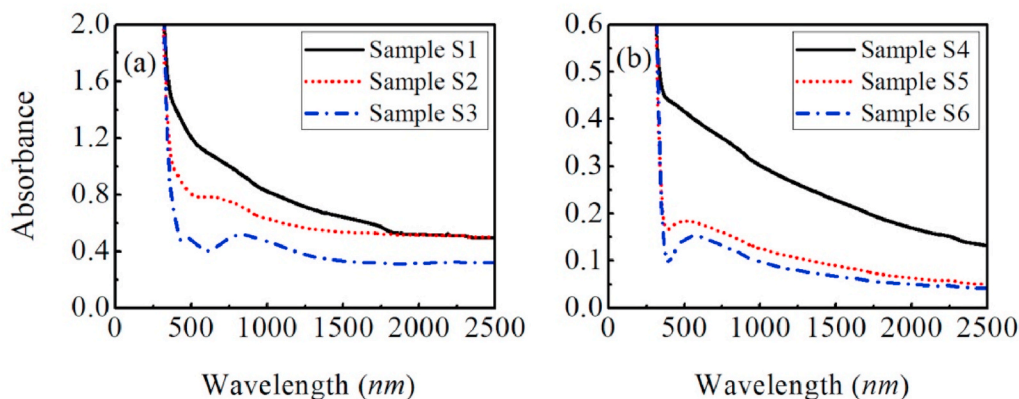
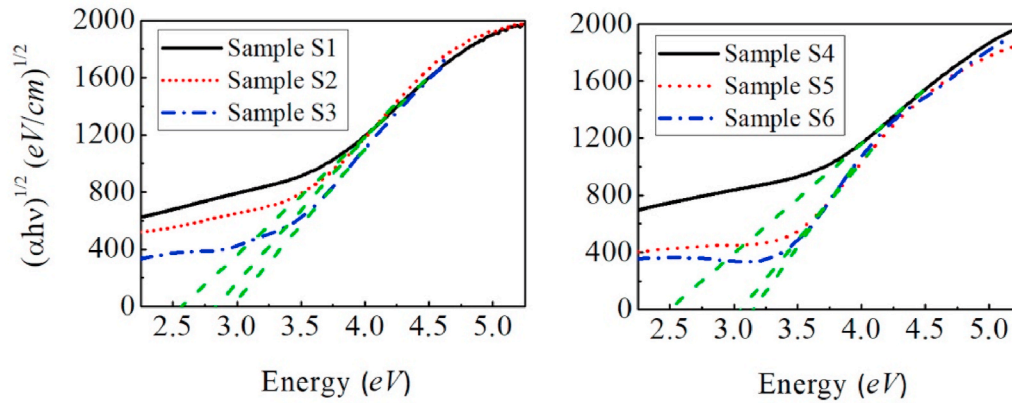


Fig. 5. Absorbance spectra in the UV-VIS-NIR range for the *as-deposited* and annealed films. (a): thicker set; (b) thinner set. (no colour printing required). (For interpretation of the references to colour in this figure legend, the reader is referred to the Web version of this article.)



**Fig. 6.** Tauc plots of  $\text{WO}_{3-x}$  films before and after annealing. The intersection of the fitting line with the x-axis provides an estimate for the bandgap energy  $E_g$ . Numerical results are reported in Table 1. (no colour printing required). (For interpretation of the references to colour in this figure legend, the reader is referred to the Web version of this article.)

temperature (400 °C) leads to more transparent films than those annealed at lower temperature (300 °C). In particular, both values  $E_g = 3.05$  eV (S5) and  $E_g = 3.15$  eV (S6) are consistent with optical bandgaps of fully oxidized  $\text{WO}_3$  [11]. In summary, by proceeding Tauc plot analysis we can assume an indirect optical bandgap for the presently fabricated  $\text{WO}_{3-x}$  films. Details of fitting procedure used for extrapolating  $E_g$  values and a discussion about the accuracy and reliability of Tauc method are given in Appendix A. As explained therein, after choosing a suitable energy midpoint for the linear fitting window of the absorption curves, the value of  $E_g$  can be estimated within an accuracy of about  $\pm 0.01$  eV, in dependence on the chosen width of the linear fitting window. With this result we contribute to the debate about reliability of Tauc plot method in processing absorption data for the value of optical bandgap, substantially confirming the most supportive conclusions [77].

From what expressed so far, it is evident that the more disruptive effects on optical absorbance and bandgap are introduced by annealing at 300 °C. As the annealing temperature increases to 400 °C, changes can be considered as incremental, as  $E_g$  widens and transparency is furtherly enhanced in both sets of films. One possible explanation for this behavior is that, during the process of film oxidation at 300 °C, oxygen incorporation causes a decrease in oxygen vacancy concentration. Eventually self-doping due to intrinsic defects is reduced. This in turn lowers the population of free carriers and weakens its residual contribution to optical absorption in the NIR. Saturation in stoichiometry causes a blue shift of absorption edge and a broadening of bandgap, so that the film transparency increases in the visible range. Between 300 °C and 400 °C crystallization occurs at saturated stoichiometry, with minor incremental effects on the transparency range.

### 3.3. Dielectric response in the UV-VIS-NIR

The optical properties of differently processed  $\text{WO}_{3-x}$  layers are fully characterized by the values of wavelength dependent complex dielectric function  $\tilde{\epsilon}(\lambda) = \epsilon_1(\lambda) + i\epsilon_2(\lambda)$  and complex refractive index  $\tilde{n}(\lambda) = n(\lambda) + ik(\lambda)$ , as obtained from VASE analysis in the UV-VIS-NIR spectral range for samples S4, S5 and S6 on Si (100) substrates. The back surface of Si wafer was roughened so that backside optical reflections are avoided. The resulting multi-layered stack of films was modelled as shown in Fig. 7. Native oxide on Si wafer was accounted for by adding a 2 nm-thick layer of  $\text{SiO}_2$  at the top surface of the substrate. The optical constants for silicon and silica were provided by the software database and taken from literature. Tungsten oxide films were modelled by suitable parametric representations of their dielectric functions, on a case-by-case basis as described hereafter. To account for surface roughness, a linear effective medium approximation (EMA) layer [78] was added at

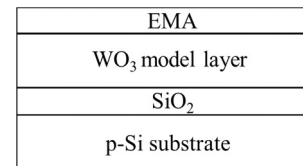


**Fig. 7.** A simple scheme of the stack of layers in ellipsometric model. (no colour printing required).

top, by assuming 50%  $\text{WO}_{3-x}$  and 50% void. All layers were supposed to be homogenous. In modelling amorphous S4 and S5 films, isotropic  $\text{WO}_{3-x}$  layers were considered. In case of crystalline monoclinic sample S6, we built models under the assumption of optical anisotropy.

Fig. 8 compares experimental data ( $\Psi$  and  $\Delta$ ) for the three samples S4, S5 and S6, taken over the spectral range 350 nm–1700 nm at angles of incidence 65°, 70° and 75°, and generated data from corresponding models. The agreement between fit and experiment is quite good. For each film sample, a specific fitting model layer is built, to represent its specific dielectric behavior. Fitting strategies are described in the following content of this section and best-fit values of parameters are collected in Table 3.

The dielectric model for sample S4 (which is strongly absorptive), was built by initially assuming a fixed guess for the thickness ( $d = 55$  nm) and by directly inverting the experimental data ( $\Psi$ ,  $\Delta$ ) in the range 800–1700 nm to obtain  $n$  and  $\kappa$  (normal fit). The tabulated values for  $n$  and  $\kappa$  were saved as a reference to fit a general oscillator model for  $\epsilon_1$ ,  $\epsilon_2$  and thickness  $d$ . After obtaining a good fit within the 800–1700 nm range using two Gaussian oscillators, a Tauc-Lorentz oscillator [79] was added to account for the dispersion of optical constants at shorter wavelengths around the optical bandgap. In Tauc-Lorentz model, the imaginary part ( $\epsilon_2$ ) of the dielectric function can be described as [80]:

$$\epsilon_2(E) = \frac{DE_n\Gamma(E - E_g)^2}{E[(E^2 - E_n^2)^2 + \Gamma^2E^2]} \Theta(E - E_g) \quad (4)$$

where  $E$  is the photon energy,  $E_g$  is the bandgap of the material,  $E_n$  is the peak transition energy,  $\Gamma$  is the broadening parameter,  $D$  is a prefactor which includes the optical transition matrix elements, and  $\Theta$  is the Heaviside step function, where  $\Theta(E - E_g < 0) = 0$  and  $\Theta(E - E_g \geq 0) = 1$ .

The real part of Tauc-Lorentz dielectric function is obtained by Kramers-Kronig transform of  $\epsilon_2(E)$  as [81]:

$$\epsilon_1(E) = \epsilon_1(\infty) + \frac{2}{\pi} P \int_{E_g}^{\infty} \frac{\xi \epsilon_2(\xi)}{\xi^2 - E^2} d\xi \quad (5)$$

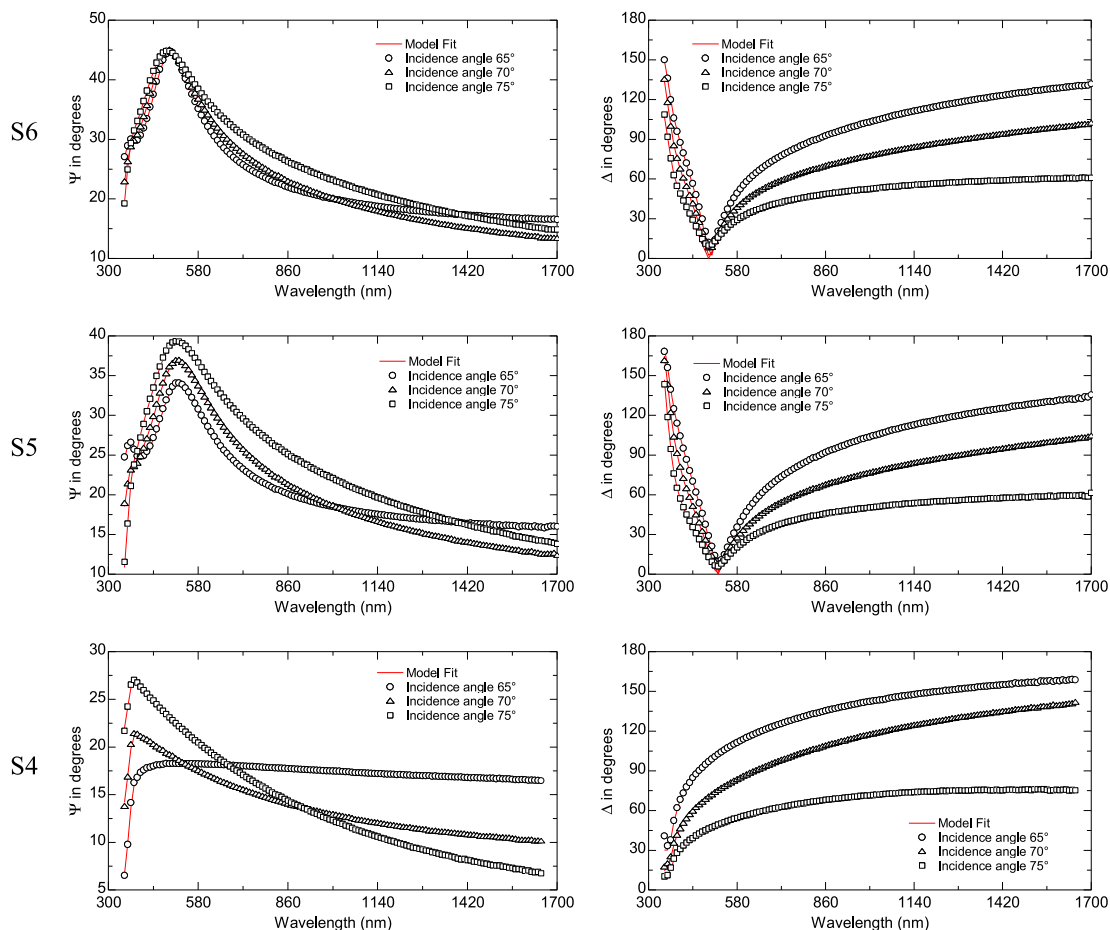


**Fig. 8.** Experimental spectral ellipsometric data ( $\Psi$  and  $\Delta$  and the model fittings at the indicated incidence angles for samples S4, S5, and S6. (no colour printing required). (For interpretation of the references to colour in this figure legend, the reader is referred to the Web version of this article.)

**Table 3**  
Ellipsometric parameters for fitting S4, S5 and S6.

Gaussian + Tauc-Lorentz		Cauchy-Urbach		
Parameters	S4	Parameters	S5	S6
MSE	2.773	MSE	5.554	3.287
D(eV)	53.243	$A'$	1.9893	2.0357
$E_n$ (eV)	4.9614	$B'$	0.010188	0.032761
$E_g$ (eV)	2.2099	$C'$	0.0034772	0.0033005
$\Gamma$ (eV)	3.2697	$\eta$	0.042184	0.050275
Pole 1(eV)	6.2333	$\delta$	5.9537	2.1026
Magnitude 1	0	$\gamma$ (nm)	400	400
Pole 2(eV)	0.001	$\varphi$	–	–15.508
Magnitude 2	0.19735	$\theta$	–	68.221
$\epsilon_1$ offset(eV)	2.0405	$\psi$	–	8.3921
EMA (nm)	–	EMA (nm)	6.4	–
thickness(nm)	50.7	thickness(nm)	61.6	63.9

where  $\epsilon_1(\infty)$  is the offset value of real part of dielectric function at high frequencies, and  $P$  stands for the Cauchy principal value of the integral. The final model provides a very good agreement (MSE = 2.773) between fitted and experimental  $\Psi$ ,  $\Delta$  over the whole spectral range (350–1700 nm), with thickness  $d = 50.7$  nm and negligible surface roughness, fully according with morphological SEM and AFM characterizations.

Samples S5 and S6 were modelled by referring to the results of Tauc analysis, which illustrates a virtually non-absorbing behavior in the VIS and NIR range. For sample S5 we selected 700 nm–1700 nm as a

transparent range and fitted the ellipsometric data for the refractive index, the film thickness, and the film roughness by assuming a Cauchy dispersion relation [82]. In Cauchy model, zero absorption ( $\kappa \cong 0$ ) is assumed and the real part of the refractive index is described by the power-law dispersion relation:

$$n(\lambda) = A' + \frac{B'}{\lambda^2} + \frac{C'}{\lambda^4} + \dots \quad (6)$$

where  $A'$ ,  $B'$  and  $C'$  are the fitting parameters, which express respectively a reference value for  $n$  and dispersion curvature. Positive values for  $A'$ ,  $B'$  and  $C'$  describe normal dispersion condition, being  $n(\lambda)$  a decreasing function of wavelength. The model has been refined by adding an exponential Urbach absorption tail [83] to model the extinction coefficient  $\kappa$  near the band edge, as:

$$\kappa(\lambda) = \eta \exp \left[ \delta \left( \frac{1}{\lambda} - \frac{1}{\gamma} \right) \right] \quad (7)$$

where  $\eta$  and  $\delta$  are respectively the amplitude and exponent, and  $\gamma$  is the band edge, which is assumed to be at 400 nm for reference. Values of the best fitting parameters are reported in Table 3. Film thickness  $d = 61.6$  nm and a surface roughness thickness of 6.4 nm, which can be considered as consistent with peak-to-peak average results obtained from other techniques.

Fig. 9 shows the dispersion of optical constants  $n$  and  $\kappa$  for three films. In case of *as-deposited* sample S4,  $n$  shows anomalous chromatic dispersion starting from about 400 nm and increases with wavelength, from 2.37 at  $\lambda = 550$  nm to a value of around 2.90 at  $\lambda = 1600$  nm.

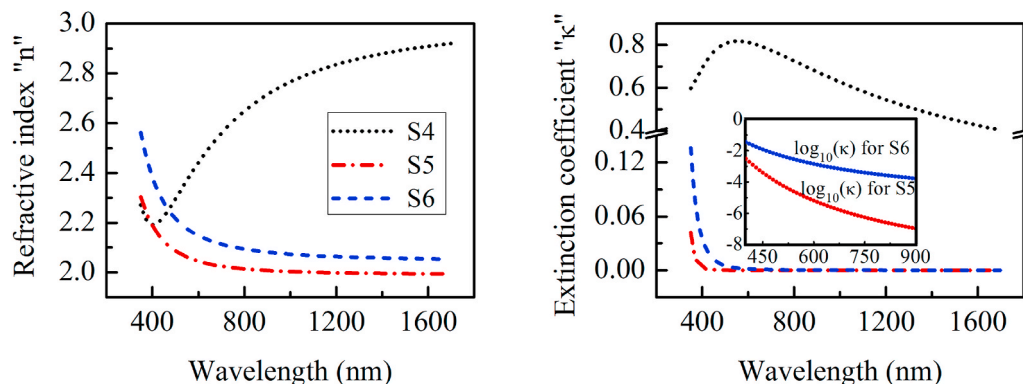


**Fig. 9.** Spectral refractive index  $n$  and extinction coefficient  $\kappa$  for  $\text{WO}_{3-x}$  thin films (samples S4, S5 and S6) by ellipsometry. In the right, an inset accounting for the  $\log_{10}(\kappa)$  is added. (no colour printing required). (For interpretation of the references to colour in this figure legend, the reader is referred to the Web version of this article.)

Correspondingly,  $\kappa$  is peaked at  $\lambda \approx 550$  nm, though it is large over the whole measured spectral range. This peculiar spectral behavior qualitatively matches ellipsometric results reported by Xin et al. for  $n(\lambda)$  in sub-stoichiometric  $\text{WO}_{3-x}$  thin films [84] and is likely to be related to the occurrence of an absorption structure in the NIR or SWIR beyond the present range. In the case of absorbing opaque films, ellipsometric data  $\Psi$  and  $\Delta$  generally do not show the strong spectral features that are typical of transparent films, as it is also evident in Fig. 8, by comparing results from sample S4 to S5 and S6. This fact may reduce the precision in fitting and finally lead to errors in estimating  $n$  and  $\kappa$ . For this reason, in the present study several runs of experimental data were taken and fitted by using different models and functional forms of  $\epsilon_2$ . The results presented here are representative of best fitting outputs. Both annealed samples S5 and S6, which are more transparent, show a normal chromatic dispersion. In case of amorphous S5 film, the single-valued  $n$  decreases from 2.06 @550 nm to 1.99 @1600 nm, while  $\kappa$  is practically negligible over the whole spectral range except towards the bandgap in the near UV, according to Urbach absorption tail and also in substantial agreement with results published in Refs. [6,76,85]. The case of S6 sample, which is anisotropic, deserves a deeper discussion. When the birefringent nature of crystalline  $\text{WO}_{3-x}$  films is neglected, ellipsometry issues an average value for wavelength-dependent refractive index as in Fig. 9. In particular, by comparing ( $n, \kappa$ ) results for the three samples reported therein, it is evident that the average refractive index for S6 (e.g.,  $n = 2.17$  @550 nm and  $n = 2.05$  @1600 nm) is higher than that of S5. This configuration is in accordance with some theoretical calculations [6] and previously reported ellipsometric characterization [76], claiming a lowering in refractive index for less stoichiometric films in presence of oxygen vacancies and related decrease in mass density. The real ( $\epsilon_1(\lambda)$ ) and imaginary ( $\epsilon_2(\lambda)$ ) parts of dielectric function were also calculated, which show equivalent spectral features to the corresponding  $n(\lambda)$  and  $\kappa(\lambda)$ , and have not been reported.

By inspection of extinction coefficient in Fig. 9, it is evident that thermal annealing in air is effective in drastically reducing optical absorption, so that films can be considered as completely transparent to the NIR. The spectrum for  $\kappa(\lambda)$  is zoomed-in on a logarithmic scale in the inset. Values of  $\kappa_{S5} = 4.0 \times 10^{-9}$  and  $\kappa_{S6} = 3.0 \times 10^{-5}$  are estimated at  $\lambda = 1500$  nm, respectively for sample S5 and S6, meaning that films can be considered as completely dielectric in the NIR range.

A deeper insight into the dielectric properties of the crystallized S6 film is provided by accounting for its optical anisotropy. Results of XRD analysis shows that S6 film on Si (001), after annealing at 400 °C and subsequent cooling down to RT, is polycrystalline with monoclinic phases preferably oriented along (002) direction (c-axis), though other orientations are also detected. Monoclinic bulk  $\text{WO}_3$  is naturally a biaxially birefringent crystal [86] and the principal values for refractive indices have been measured in the visible range as  $n_a = 2.703$ ,  $n_b =$

2.376,  $n_c = 2.283$ , with an average value of  $\bar{n} = 2.454$  [87]. In this work we have characterized the birefringence of crystalline  $\text{WO}_{3-x}$  film S6, by fitting ellipsometric data to an anisotropic model. We retain the hypothesis of biaxial optical birefringence, compatible with monoclinic symmetry of the films as shown by XRD analysis. For biaxial fitting, the  $\text{WO}_{3-x}$  film is modelled as a Cauchy layer with Urbach absorption tail, and birefringence is expressed by adding non-dispersive increments to the refractive index for light polarized along the principal directions  $x, y, z$  referenced to the plane of optical incidence, as shown in Fig. 10.

This approach neglects any anisotropy in absorption coefficient. The coefficients of Cauchy-Urbach model, the increments  $\Delta n_{x,y,z}$  and the film thickness are free fitting parameters. Effective values for the refractive indices are expected, as averaged contributions from mixed orientations of the crystallites. The relative orientation of the optical indicatrix for monoclinic  $\text{WO}_3$  with respect to the direction of film normal to the optical plane of incidence is also fitted and expressed by the values of Euler angles ( $\varphi, \theta, \psi$ ). Best fitting ellipsometric parameters for S6 are shown in Table 3. In particular, zero thickness for the EMA roughness layer is obtained, thus indicating that crystallization leads to very high optical quality. Fig. 11 plots normal spectral dispersion of reference indices  $n_{x,y,z}$  as resulting from ellipsometry analysis. Also in this case, absorption is negligible in the NIR and is quantified in the inset on a logarithmic scale. The condition  $n_x > n_y > n_z$  agrees with that of the optical indicatrix for bulk monoclinic tungsten oxide [87] and matches with XRD indications for a preferential c-axis orientation of sample S6. The lower values of

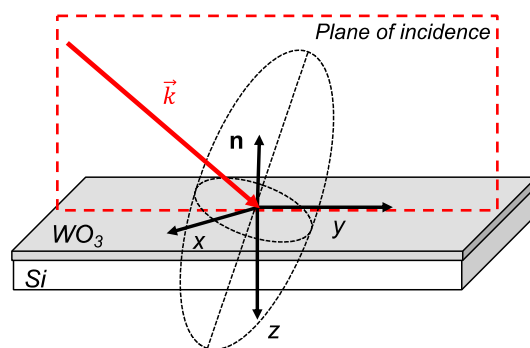


**Fig. 10.** A scheme of reference geometry for biaxial fitting by ellipsometry. The  $\text{WO}_3$  film on Si substrate is shown, with its normal direction  $\mathbf{n}$ . The direction of light wavevector  $\vec{k}$  is marked. Perpendicular directions  $x, y, z$  are taken respectively as orthogonal to the incidence plane (s-polarization), in the plane of incidence (p-polarization) and in the negative normal direction of the film. A generically oriented optical indicatrix for the film is also indicated. (no colour printing required). (For interpretation of the references to colour in this figure legend, the reader is referred to the Web version of this article.)

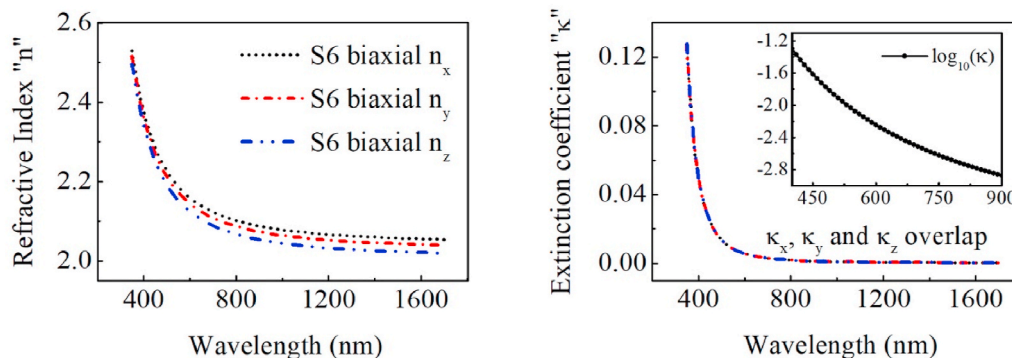


**Fig. 11.** Plots refractive index  $n$  and extinction coefficient  $\kappa$  for S6 in biaxial consideration. In the right, an inset accounting for the  $\log_{10}(\kappa)$  is added. Anisotropy in absorption is neglected. (no colour printing required). (For interpretation of the references to colour in this figure legend, the reader is referred to the Web version of this article.)

refractive indices for the film with respect to bulk  $\text{WO}_3$  ( $n_x = 2.188$ ,  $n_y = 2.172$ ,  $n_z = 2.152$  in visible light) can be justified by claiming a less dense material. However, it is also worth recalling that ellipsometry measures the effective birefringence globally expressed by the polycrystalline film, which is a macroscopic averaging of the contributions from the single crystallites. Therefore, in any case the values for  $n_{x,y,z}$  are to be taken as equivalent parameters that represent the refractive properties of the film. In this regard, for light at  $\lambda = 1500$  nm and at normal incidence, by considering experimental values of  $n_x = 2.0581$ ,  $n_y = 2.0437$ , S6 film ( $d = 63$  nm) would behave as a retarding waveplate of relative retarding power  $\Delta\varphi = \frac{2\pi}{\lambda} \cdot d \cdot \Delta n_{x,y} = 0.22$  deg.

In summary, high transparency in the IR range emerges as a key feature of the annealed deposited films both from absorption spectroscopy and from ellipsometry. Also in the case of *as-deposited* S1 and S4 samples, we remark that in present work the NIR absorption tail is absent for  $\text{WO}_{3-x}$  films, where the NIR absorption is associated to free carriers and would be expected as typical of sub-stoichiometric  $\text{WO}_{3-x}$  films [68].

### 3.4. Integrating $\text{WO}_{3-x}$ film in 1D resonant structure

The transmittance of the multilayer  $\text{SiO}_2/\text{TiO}_2$  1D-PBG over the whole 210 nm–1800 nm spectrum is plotted in Fig. 12. In the final geometry, transmission from 890 nm to 1450 nm was minimized in a

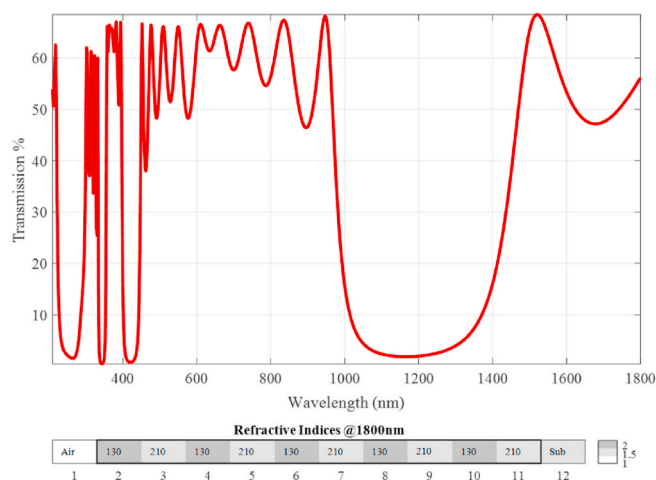


**Fig. 12.** Upper: transmission spectrum of the multilayer from 210 nm to 1800 nm with the step size of 2 nm; Lower: multilayer design configuration. (no colour printing required). (For interpretation of the references to colour in this figure legend, the reader is referred to the Web version of this article.)

structure formed by five pairs of alternating  $\text{TiO}_2$  (refractive index  $n \sim 2$ ) and  $\text{SiO}_2$  (refractive index  $n \sim 1.5$ ) thin-film layers with thicknesses of 210 nm and 130 nm, respectively (Fig. 12 at bottom).

The effectiveness of the 1D-PBG structure in enhancing optical field at  $\text{WO}_{3-x}$  surface is summarized in Fig. 13, which shows that the standard reflection/transmission ratio of a single  $\text{WO}_{3-x}$  film on silica substrate (Fig. 13a) is enhanced by four times in the case of  $\text{WO}_{3-x}$ -PBG (Fig. 13b).

The localization of optical field in  $\text{WO}_{3-x}$  layer was studied by FEM and the spatial distribution of normalized amplitude of the associated electric field was calculated throughout the structure at band-edge wavelengths (10 nm-steps from 1400 nm to 1700 nm). In order to determine the ideal thickness of the  $\text{WO}_{3-x}$  layer, a parametric study was performed by letting the thickness sweeping from 100 nm to 500 nm with an increment size of 10 nm. The maximum electric field concentration was obtained with a 450 nm-thick  $\text{WO}_{3-x}$  layer. Fig. 14a plots the norm of electric field amplitude over all the layers of 1D-PBG (i.e.,  $5 \times (\text{SiO}_2/\text{TiO}_2)$  and 450 nm-thick top  $\text{WO}_{3-x}$  layer), calculated over the NIR spectral range 1400 nm–1700 nm that comprises the band-edges. At  $\lambda = 1416$  nm a definite growth in electric field amplitude occurs in correspondence with the  $\text{WO}_{3-x}$  layer. A 3D distribution of the absolute value of optical field amplitude in the volume of dielectric structure is reported in Fig. 14b. It is evident that the multilayer stack acts in confining incident light mostly within the  $\text{WO}_{3-x}$  layer at top. The maximum field amplitude is obtained at the surface of the structure.

## 4. Conclusions

Compact  $\text{WO}_{3-x}$  thin films have been fabricated from a  $\text{WO}_3$  target by a non-reactive RF-sputtering deposition process at RT in Ar atmosphere, followed by 8 h of thermal annealing in dry air at ambient pressure. Films are transparent in the near and short-wavelength infrared spectral range. By selecting the duration of deposition, two sets of differently thick films have been obtained. *As-deposited* films are amorphous, sub-stoichiometric, optically opaque in the visible range and electrically conductive. The bandgap has been evaluated from optical absorption spectroscopy, by a detailed implementation of Tauc plot method and  $E_g$  values of 2.57 eV and 2.49 eV are obtained, respectively for the thicker (around 200 nm) and thinner (around 60 nm) sets. Thermal annealing strongly improves optical transparency and widens energy bandgap, both effects being an increasing function of annealing temperature. Annealing at 300 °C keeps the films amorphous, with  $E_g = 2.84$  eV and 3.05 eV (thicker and thinner case, respectively). The threshold for crystallization is exceeded when heating at 400 °C and polycrystalline  $\text{WO}_3$  films in monoclinic phase are obtained after cooling down to normal conditions. The  $E_g$  for crystallized samples measures respectively 2.96 eV and 3.15 eV, for thicker and thinner films. Bandgap values

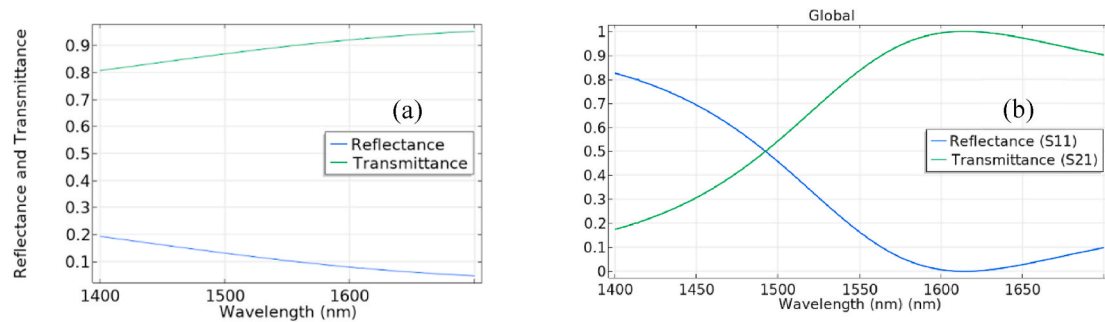


**Fig. 13.** Optical reflection and transmission at a 450 nm-thick  $\text{WO}_{3-x}$  film: (a) the case of a single  $\text{WO}_{3-x}$  layer on a  $\text{SiO}_2$  substrate in air; (b) Optical reflection and transmission in the case of a 450 nm-thick  $\text{WO}_{3-x}$  film on top of the 1D-PBG multilayer. (colour printing required). (For interpretation of the references to colour in this figure legend, the reader is referred to the Web version of this article.)

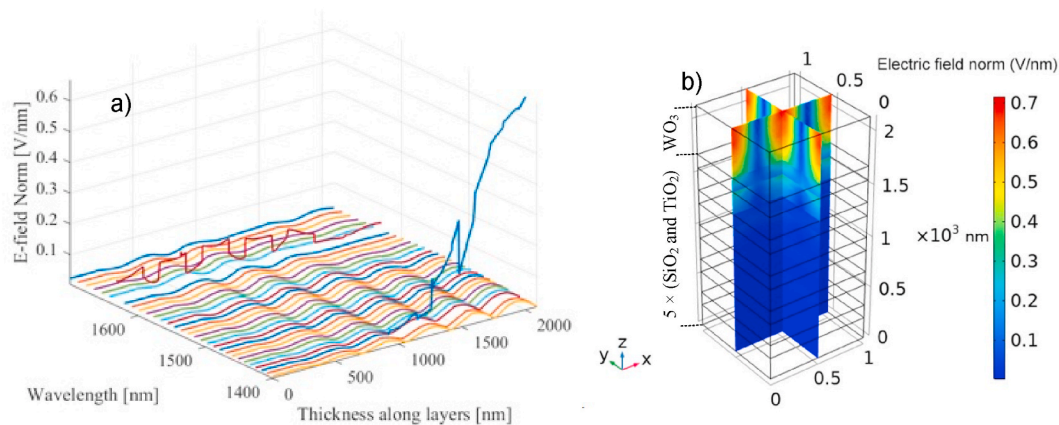


**Fig. 14.** (a): Electric field norm distribution throughout the whole multilayer structure ( $5 \times (\text{SiO}_2/\text{TiO}_2) + 450 \text{ nm}$  of  $\text{WO}_{3-x}$  layer) at the band-edge wavelengths; (b): an 3D representation of the distribution of electric field amplitude at 1416 nm, showing the localization within the of the  $\text{WO}_{3-x}$  layer. (colour printing required). (For interpretation of the references to colour in this figure legend, the reader is referred to the Web version of this article.)

suggest that in case of thinner films almost perfect stoichiometry is obtained. This is also suggested by XRD results on crystallized samples, even if XPS measurement may indicate that, in case of thicker films sub-stoichiometric coordination is still present at film surface. Average surface roughness keeps low values (in the few nm range), both in as-grown and annealed films, thus indicating good optical quality. The degree of smoothness and compactness of films is compatible with applications to coherent processing of optical field in amplitude and phase. Over the 350 nm-1700 nm spectral interval, *as-deposited*  $\text{WO}_{3-x}$  films show a complex refractive index  $\tilde{n}(\lambda)$  typical of opaque layers, with finite values for  $\kappa(\lambda)$  peaked at around  $\lambda = 550 \text{ nm}$  and anomalous dispersion for  $n(\lambda)$ . Values as high as  $n(\lambda) \sim 2.9$  are estimated in the NIR. On the contrary, annealed films look dielectric, with normal chromatic dispersion for  $n(\lambda)$  and very low absorption. The peculiar feature of these compact and optical-grade  $\text{WO}_{3-x}$  films is the absence of the absorption tail in the NIR, which is the characteristic contribution and footprint of free conduction electrons. In case of annealed samples, the region of negligible absorption extends to the NIR and SWIR spectral range, with refractive index values close to 1.95~2.1. This opens the possibility to embed  $\text{WO}_{3-x}$  films into multi-layered infrared resonant photonic structures for sensing application. The preliminary design presently introduced of a silica-titania 1D-PBG capped with a  $\text{WO}_{3-x}$  layer confirms that incident light at 1416 nm is localized in the topmost  $\text{WO}_{3-x}$ . Future exploration of optical sensors in the NIR using tungsten oxide thin films could be developed with the current work as a cornerstone.

#### CRediT authorship contribution statement

**Hao Chen:** Conceptualization, Investigation, (SEM, profilometry, ellipsometry), Formal analysis, Writing – original draft, preparation. **Alessandro Chiasera:** Investigation, (RF-sputtering, optical spectroscopy). **Stefano Varas:** Resources, Investigation, (RF sputtering, optical spectroscopy). **Osman Sayginer:** Investigation, (RF sputtering, optical spectroscopy), Software, (FEM modelling). **Cristina Armellini:** Investigation, (XRD), Conceptualization, Supervision, Writing – review & editing/Writing-Reviewing and Editing. **Giorgio Speranza:** Investigation, (XPS). **Raffaella Suriano:** Investigation, (AFM). **Maurizio Ferrari:** Conceptualization. **Silvia Maria Pietralunga:** Conceptualization, Supervision, Writing – review & editing/Writing-Reviewing and Editing.

#### Declaration of competing interest

The authors declare that they have no known competing financial interests or personal relationships that could have appeared to influence the work reported in this paper.

#### Acknowledgement

Authors acknowledge co-funding of research by European fund - FESR, PON Ricerca e Innovazione 2014–2020, Project ARS01\_00519.

## Appendix A. Tauc plot calculation of optical bandgap

We discuss here the accuracy and reliability of Tauc method in obtaining  $E_g$  values. An entirely unbiased way [88] of picking sequential datapoints from the linear portion of absorption curves was applied for the purpose of performing linear regressions. Three different windows, each one respectively comprising 7, 15, and 27 sequential datapoints were selected for comparison (e.g., “7 data points” means 3 datapoints on either side of a midpoint). The quality of linear fitting is expressed by the coefficient of determination ( $R^2$ ): the more the  $R^2$  approaches unity, the better is the fit and the more accurate is  $E_g$  extrapolation. Results are shown in Figure A.1 and Figure A.2. By fitting over a 7-datapoint window,  $R^2$  approaches unity over a wide energy range, indicating its insufficiency to identify the optimal region of absorption curves for linear fitting, so that inaccurate extrapolated  $E_g$  values may result. As the datapoints range increases, a definite maximum in  $R^2$  is observed. The energy value that maximizes  $R^2$  is the best energy midpoint to locate the linear fitting window for bandgap extrapolation. However, larger sizes of datapoints also imply larger deviations of experimental data from the regression line. In other words, an overmuch large window of datapoints is likely to worsen the fitting quality. For example, this phenomenon is evident in the case of sample S6, where the value of  $R^2$  decreases in correspondence to the widest (27 datapoints) range. The extrapolated values for  $E_g$  depend on the choice of the energy midpoint and of the width of the fitting datapoint window, as visually shown in Figure A.2(b). Specifically, at the best midpoint for linear regression, the extrapolated values of  $E_g$  differ by about 0.01 eV, in dependence on the size of selected datapoint range. We can therefore say that Tauc plot method estimates the optical bandgap  $E_g$  within an ultimate accuracy of about  $\pm 0.01$  eV, which mainly depends on the chosen width of the linear fitting window, after performing a rigorous statistical analysis to identify the best fitting midpoint.

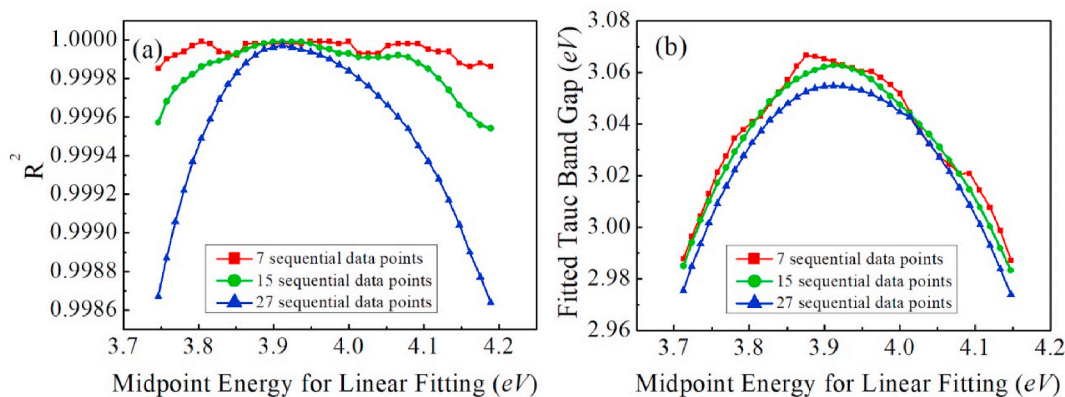


Fig. A.1. (a): Linear regression fitting quality for different portions of the data from sample S5. (b): The corresponding fitted Tauc band gap obtained from linear regressions. (no colour printing required).

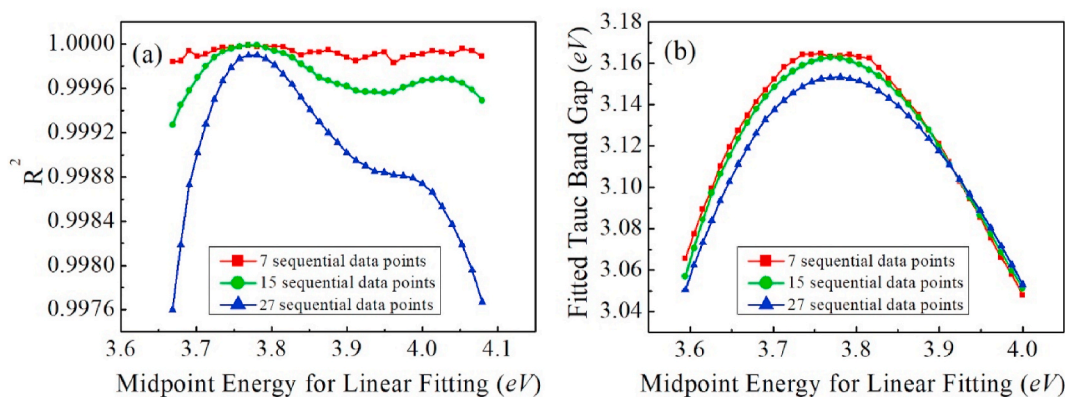


Fig. A.2. (a): Linear regression fitting quality for different portions of the data from sample S6. (b): The corresponding fitted Tauc band gap obtained from linear regressions. (no colour printing required).

## APPENDIX B. Notes on Variable Angle Spectroscopic Ellipsometry

The complex dielectric function is expressed as  $\tilde{\epsilon}(\lambda) = \epsilon_1(\lambda) + i\epsilon_2(\lambda)$ , where the real part  $\epsilon_1(\lambda)$  expresses the evolution of phase of optical field in propagation at negligible absorption, and the imaginary part  $\epsilon_2(\lambda)$  is related to optical absorbance. The real and imaginary part of the dielectric function mutually transform one into the other by Kramers-Kronig relations [81]. The complex dielectric function is related to the complex refractive index  $\tilde{n}(\lambda) = n(\lambda) + i\kappa(\lambda)$  as  $\epsilon_1 = n^2 - \kappa^2$  and  $\epsilon_2 = 2n\kappa$ , where  $\kappa(\lambda) = \alpha(\lambda) \cdot \lambda / 4\pi$  is the extinction coefficient, and the real part of the refractive index  $n(\lambda)$  contributes to optical phase retardation in propagation. Upon crystallization, optical materials switch from being isotropic to anisotropic, so that the dielectric parameters  $\tilde{\epsilon}(\lambda), \tilde{n}(\lambda)$  have to be generally expressed in tensorial forms, according to specific crystalline symmetry groups [86].

Variable Angle spectroscopic Ellipsometry (VASE) is based on detecting the change in polarization of light upon reflection from samples under test, as a function of wavelength and incidence angle  $(\lambda, \theta)$ . Samples can be either optically thick films (bare substrates) or transparent films on substrates and multi-layered stacks. What is measured is the complex ratio  $\tilde{\rho}$  of the Fresnel reflection coefficients for light being polarized respectively parallel ( $r_p$ ) and orthogonal ( $r_s$ ) to the plane of incidence, that can be expressed in amplitude ratio ( $\Psi$ ) and phase difference ( $\Delta$ ) as:

$$\tilde{\rho} = \tan(\Psi(\theta, \lambda)) \exp(i\Delta(\theta, \lambda)) = \frac{r_p(\theta, \lambda)}{r_s(\theta, \lambda)} \quad (8)$$

where angles ( $\Psi$ ) and ( $\Delta$ ) are real quantities. For samples based on stacked thin films,  $\tilde{\rho}$  is a function of the refractive indices and absorption coefficients of the films as well as of their thicknesses. In principle, by inverting  $r_p$  and  $r_s$  (or  $\Psi$  and  $\Delta$ ) one can obtain  $n(\lambda)$  and  $\kappa(\lambda)$ , or equivalently  $\varepsilon_1(\lambda)$  and  $\varepsilon_2(\lambda)$ . In practical cases, the optical constants are evaluated by performing a multivariate non-linear regression analysis of ellipsometric data. An appropriate fitting model for the sample under test must be developed, which includes parametric expressions for the complex dielectric functions and the thickness of all the layers, and which is refined by fitting for morphological and structural information such as porosity, surface roughness, homogeneity, and anisotropy.

## References

- C.C. Mardare, A.W. Hassel, Review on the versatility of tungsten oxide coatings, *Phys. Status Solidi Appl. Mater. Sci.* 216 (2019), 1900047, <https://doi.org/10.1002/pssa.201900047>.
- A. Al Mohammad, M. Gillet, Phase transformations in WO3 thin films during annealing, *Thin Solid Films* 408 (2002) 302–309, [https://doi.org/10.1016/S0040-6090\(02\)00090-1](https://doi.org/10.1016/S0040-6090(02)00090-1).
- E. Salje, K. Viswanathan, Physical properties and phase transitions in WO3, *Acta Crystallogr. A* A31 (1975) 356–359, <https://doi.org/10.1107/S0567739475000745>.
- C.J. Howard, V. Luca, K.S. Knight, High-temperature phase transitions in tungsten trioxide—the last word? *J. Phys. Condens. Matter* 14 (2002) 377–387, <https://doi.org/10.1088/0953-8984/14/3/308>.
- D.B. Migas, V.L. Shaposhnikov, V.E. Borisenko, Tungsten oxides. II. The metallic nature of Magnil phases, *J. Appl. Phys.* 108 (2010), 093714, <https://doi.org/10.1063/1.3505689>.
- F. Mehmood, R. Pachter, N.R. Murphy, W.E. Johnson, C.V. Ramana, Effect of oxygen vacancies on the electronic and optical properties of tungsten oxide from first principles calculations, *J. Appl. Phys.* 120 (2016), 233105, <https://doi.org/10.1063/1.4972038>.
- D.B. Migas, V.L. Shaposhnikov, V.N. Rodin, V.E. Borisenko, Tungsten oxides. I. Effects of oxygen vacancies and doping on electronic and optical properties of different phases of WO3, *J. Appl. Phys.* 108 (2010), 093713, <https://doi.org/10.1063/1.3505688>.
- F. Wang, C. Di Valentin, G. Pacchioni, Semiconductor-to-metal transition in WO3-x: nature of the oxygen vacancy, *Phys. Rev. B Condens. Matter* 84 (2011) 1–5, <https://doi.org/10.1103/PhysRevB.84.073103>.
- D. Dellasega, S.M. Pietralunga, A. Pezzoli, V. Russo, L. Nasi, C. Conti, M.J. Vahid, A. Tagliaferri, M. Passoni, Tungsten oxide nanowires grown on amorphous-like tungsten films, *Nanotechnology* 26 (2015) 365601, <https://doi.org/10.1088/0957-4484/26/36/365601>.
- D. Lu, B. Liang, A. Ogino, M. Nagatsu, Study of the synthesis of tungsten trioxide nanostructured arrays by tungsten hot filament chemical vapor deposition method and their field emission properties, *J. Vac. Sci. Technol. B* 28 (2010) C2A98–C2A103, <https://doi.org/10.1116/1.3292599>.
- C.G. Granqvist, *Handbook of Inorganic Electrochromic Materials*, Elsevier Science, 1995, <https://doi.org/10.1016/B978-0-444-89930-9.X5000-4>.
- E. Washizu, A. Yamamoto, Y. Abe, M. Kawamura, K. Sasaki, Optical and electrochromic properties of RF reactively sputtered WO3 films, *Solid State Ionics* 165 (2003) 175–180, <https://doi.org/10.1016/j.ssi.2003.08.030>.
- H. Kaneko, S. Nishimoto, K. Miyake, N. Suedomi, Physical and electrochromic properties of rf sputtered tungsten oxide films, *J. Appl. Phys.* 59 (1986) 2526–2534, <https://doi.org/10.1063/1.337001>.
- Y.C. Nah, Effects of sputter parameters on electrochromic properties of tungsten oxide thin films grown by RF sputtering, *Korean J. Mater. Res.* 21 (2011) 703–707, <https://doi.org/10.3740/MRSK.2011.21.12.703>.
- R.J. Mortimer, *Electrochromic materials*, *Annu. Rev. Mater. Res.* 41 (2011) 241–268, <https://doi.org/10.1146/annurev-matsci-062910-100344>.
- C.G. Granqvist, Electrochromic tungsten oxide films: review of progress 1993–1998, *Sol. Energy Mater. Sol. Cells* 60 (2000) 201–262, [https://doi.org/10.1016/S0927-0248\(99\)00088-4](https://doi.org/10.1016/S0927-0248(99)00088-4).
- M. Sun, N. Xu, Y.W. Cao, J.N. Yao, E.G. Wang, Nanocrystalline tungsten oxide thin film: preparation, microstructure, and photochromic behavior, *J. Mater. Res.* 15 (2000) 927–933, <https://doi.org/10.1557/JMR.2000.0132>.
- Z. He, Q. Liu, H. Hou, F. Gao, B. Tang, W. Yang, Tailored electrospinning of WO3 nanobelts as efficient ultraviolet photodetectors with photo-dark current ratios up to 1000, *ACS Appl. Mater. Interfaces* 7 (2015) 10878–10885, <https://doi.org/10.1021/acsami.5b02020>.
- B. Cook, Q. Liu, J. Butler, K. Smith, K. Shi, D. Ewing, M. Casper, A. Stramel, A. Elliot, J. Wu, Heat-Assisted inkjet printing of tungsten oxide for high-performance ultraviolet photodetectors, *ACS Appl. Mater. Interfaces* 10 (2018) 873–879, <https://doi.org/10.1021/acsami.7b15391>.
- L.B. Krikunov, D.D. Macdonald, P.J. Millett, Tungsten/tungsten oxide pH sensing electrode for high temperature aqueous environments, *J. Electrochem. Soc.* 141 (1994) 3002–3005, <https://doi.org/10.1149/1.2059272>.
- L. Santos, J.P. Neto, A. Crespo, D. Nunes, N. Costa, I.M. Fonseca, P. Barquinha, L. Pereira, J. Silva, R. Martins, E. Fortunato, WO3 nanoparticle-based conformable pH sensor, *ACS Appl. Mater. Interfaces* 6 (2014) 12226–12234, <https://doi.org/10.1021/am501724h>.
- O. Berger, T. Hoffman, W.J. Fischer, V. Melev, Tungsten-oxide thin films as novel materials with high sensitivity and selectivity to NO2, O3, and H2S. Part II: application as gas sensors, *J. Mater. Sci. Mater. Electron.* 15 (2004) 483–493, <https://doi.org/10.1023/B:JMSE.0000031602.73321.fe>.
- M. Di Giulio, D. Manno, G. Micocci, A. Serra, A. Tepore, Gas-sensing properties of sputtered thin films of tungsten oxide, *J. Phys. D Appl. Phys.* 30 (1997) 3211–3215, <https://doi.org/10.1088/0022-3727/30/23/005>.
- K. Aguir, C. Lemire, D.B.B. Lollman, Electrical properties of reactively sputtered WO3 thin films as ozone gas sensor, *Sensor. Actuator. B Chem.* 84 (2002) 1–5, [https://doi.org/10.1016/S0925-4005\(02\)00003-5](https://doi.org/10.1016/S0925-4005(02)00003-5).
- R. Boulmani, M. Bendahan, C. Lambert-Mauriat, M. Gillet, K. Aguir, Correlation between RF-sputtering parameters and WO3 sensor response towards ozone, *Sensor. Actuator. B Chem.* 125 (2007) 622–627, <https://doi.org/10.1016/j.snb.2007.03.011>.
- G.L. Chiarello, M. Bernareggi, M. Pedroni, M. Magni, S.M. Pietralunga, A. Tagliaferri, E. Vassallo, E. Selli, Enhanced photopromoted electron transfer over a bilayer WO3 n-n heterojunction prepared by RF diode sputtering, *J. Mater. Chem. A* 5 (2017) 12977, <https://doi.org/10.1039/c7ta03887a>.
- M. Pedroni, M. Canetti, G.L. Chiarello, A. Cremona, F. Inzoli, S. Luzzati, S. M. Pietralunga, A. Tagliaferri, M. Zani, E. Vassallo, Tungsten oxide thin film photoanodes by reactive RF diode sputtering, *Thin Solid Films* 616 (2016) 375–380, <https://doi.org/10.1016/j.tsf.2016.08.010>.
- Y. Yamada, K. Tabata, T. Yashima, The character of WO3 film prepared with RF sputtering, *Sol. Energy Mater. Sol. Cells* 91 (2007) 29–37, <https://doi.org/10.1016/j.solmat.2005.11.014>.
- T. Zhu, M.N. Chong, E.S. Chan, Nanostructured tungsten trioxide thin films synthesized for photoelectrocatalytic water oxidation: a review, *ChemSusChem Rev* 7 (2014) 2974–2997, <https://doi.org/10.1002/cssc.201402089>.
- Q. Yao, G. Ren, K. Xu, L. Zhu, H. Khan, M. Mohiuddin, M.W. Khan, B.Y. Zhang, A. Jannat, F. Haque, S.Z. Reza, Y. Wang, X. Wen, A. Mitchell, J.Z. Ou, 2D plasmonic tungsten oxide enabled ultrasensitive fiber optics gas sensor, *Adv. Opt. Mater.* 7 (2019) 1901383, <https://doi.org/10.1002/adom.201901383>.
- H. Zheng, J.Z. Ou, M.S. Strano, R.B. Kaner, A. Mitchell, K. Kalantar-Zadeh, Nanostructured tungsten oxide - properties, synthesis, and applications, *Adv. Funct. Mater.* 21 (2011) 2175–2196, <https://doi.org/10.1002/adfm.201002477>.
- A.K. Chawla, S. Singhal, H.O. Gupta, R. Chandra, Effect of sputtering gas on structural and optical properties of nanocrystalline tungsten oxide films, *Thin Solid Films* 517 (2008) 1042–1046, <https://doi.org/10.1016/j.tsf.2008.06.068>.
- V. RBuch, S. KRawal, A.K. Chawla, Structural, optical and electrochromic properties of sputter deposited tungsten oxide films in argon-helium atmosphere, *E-Journal Surf. Sci. Nanotechnol.* 148 (2018) 248–257, <https://doi.org/10.1380/ejssnt.2018.289>.
- M. Acosta, D. González, I. Riech, Optical properties of tungsten oxide thin films by non-reactive sputtering, *Thin Solid Films* 517 (2009) 5442–5445, <https://doi.org/10.1016/j.tsf.2009.01.090>.
- M. Acosta, R.A. Méndez, I. Riech, M. Rodríguez-Pérez, G. Rodríguez-Gattorno, Structural, optical and photoelectrochemical properties of tungsten oxide thin films grown by non-reactive RF-sputtering, *Superlattice. Microsc.* 127 (2019) 123–127, <https://doi.org/10.1016/j.spmi.2017.12.055>.
- W. Zhao, Y. Zhao, Y. Yang, J. Li, P. Lan, J. Huang, W. Song, Direct regulation of O/W stoichiometric ratio and microstructure in tungsten oxide electrochromic films by Ar pressure using oxide target sputtering, *Phys. Status Solidi* 217 (2020), 1900999, <https://doi.org/10.1002/pssa.201900999>.
- G.M. Paternò, L. Moscardi, S. Donini, D. Ariodanti, I. Kriegel, M. Zani, E. Parisini, F. Scotognella, G. Lanzani, Hybrid one-dimensional plasmonic-photonic crystals for optical detection of bacterial contaminants, *J. Phys. Chem. Lett.* 10 (2019) 4980–4986, <https://doi.org/10.1021/acs.jpclett.9b01612>.
- A. Vinante, M. Carlesso, A. Bassi, A. Chiasera, S. Varas, P. Falferi, B. Margesin, R. Mezzena, H. Ulbricht, Narrowing the parameter space of collapse models with ultracold layered force sensors, *Phys. Rev. Lett.* 125 (2020), 100404, <https://doi.org/10.1103/PhysRevLett.125.100404>.
- A. Chiasera, C. Meroni, F. Scotognella, Y.G. Boucher, G. Galzerano, A. Lukowiak, D. Ristic, G. Speranza, S. Valligatla, S. Varas, L. Zur, M. Ivanda, G.C. Righini, S. Taccheo, R. Ramponi, M. Ferrari, Coherent emission from fully Er3+ doped monolithic 1-D dielectric microcavity fabricated by rf-sputtering, *Opt. Mater.* 87 (2019) 107–111, <https://doi.org/10.1016/j.optmat.2018.04.057>.
- C.-Y. Kim, S. Park, Electrochromic properties of WO3 thin film with various heat-treatment temperature, *Asian J. Chem.* 25 (2013) 5874–5878, <https://doi.org/10.14233/ajchem.2013.oh115>.
- G. Speranza, R. Canteri, RxsPg a new open project for Photoelectron and Electron Spectroscopy data processing, *Software* 10 (2019), 100282, <https://doi.org/10.1016/j.softx.2019.100282>.

- [42] J. Tauc, Optical properties and electronic structure of amorphous Ge and Si, *Mater. Res. Bull.* 3 (1968) 37–46, [https://doi.org/10.1016/0025-5408\(68\)90023-8](https://doi.org/10.1016/0025-5408(68)90023-8).
- [43] H.G. Tompkins, E.A. Irene, *Handbook of Ellipsometry*, William Andrew Pub, Springer, 2005, <https://doi.org/10.1515/arih-2005-0022>.
- [44] G.E. Jellison Jr., Data analysis for spectroscopic ellipsometry, *Thin Solid Films* 234 (1993) 416–422, [https://doi.org/10.1016/0040-6090\(93\)90298-4](https://doi.org/10.1016/0040-6090(93)90298-4).
- [45] A. Macleod, *Thin-Film Optical Filters*, Taylor & Francis, 2012, <https://doi.org/10.1201/9781420073034>.
- [46] O. Sayginer, E. Iacob, S. Varas, A. Szcurek, M. Ferrari, A. Lukowiak, G.C. Righini, O.S. Bursi, A. Chiasera, Design, fabrication and assessment of an optomechanical sensor for pressure and vibration detection using flexible glass multilayers, *Opt. Mater.* 115 (2021), 111023, <https://doi.org/10.1016/j.optmat.2021.111023>.
- [47] O. Sayginer, A. Chiasera, L. Zur, S. Varas, L. Thi Ngoc Tran, C. Armellini, M. Ferrari, O.S. Bursi, Fabrication, modelling and assessment of hybrid 1-D elastic Fabry Perot microcavity for mechanical sensing applications, *Ceram. Int.* 45 (2019) 7785–7788, <https://doi.org/10.1016/j.ceramint.2019.01.083>.
- [48] I.H. Malitson, Interspecimen comparison of the refractive index of fused silica, *J. Opt. Soc. Am.* 55 (1965) 1205–1209, <https://doi.org/10.1364/JOSA.55.001205>.
- [49] T. Siefke, S. Kroker, K. Pfeiffer, O. Puffky, K. Dietrich, D. Franta, I. Ohlidal, A. Szeghalmi, E.-B. Kley, A. Tünnemann, Materials pushing the application limits of wire grid polarizers further into the deep ultraviolet spectral range, *Adv. Opt. Mater.* 4 (2016) 1780–1786, <https://doi.org/10.1002/adom.201600250>.
- [50] H. Chen, A. Chiasera, C. Armellini, G. Speranza, S. Varas, O. Sayginer, M. Cassinelli, M. Caironi, R. Suriano, M. Zaghoul, A. Tagliaferri, S.M. Pietralunga, Near-IR transparent conductive amorphous tungsten oxide thin layers by non-reactive radio-frequency magnetron sputtering, *Proc. EOSAM* (2021) 3–7, 2021.
- [51] H. Simchi, B.E. McCandless, T. Meng, W.N. Shafarman, Structural, optical, and surface properties of WO<sub>3</sub> thin films for solar cells, *J. Alloys Compd.* 617 (2014) 609–615, <https://doi.org/10.1016/j.jallcom.2014.08.047>.
- [52] Y.S. Zou, Y.C. Zhang, D. Lou, H.P. Wang, L. Gu, Y.H. Dong, K. Dou, X.F. Song, H. B. Zeng, Structural and optical properties of WO<sub>3</sub> films deposited by pulsed laser deposition, *J. Alloys Compd.* 583 (2014) 465–470, <https://doi.org/10.1016/j.jallcom.2013.08.166>.
- [53] B.D. Cullity, S.R. Stock, *Elements of X-Ray Diffraction*, third ed., Pearson, 2014 [https://doi.org/10.1016/0014-5793\(79\)80596-7](https://doi.org/10.1016/0014-5793(79)80596-7).
- [54] M. Tong, J. Yang, Q. Jin, X. Zhang, J. Gao, G. Li, Facile preparation of amorphous carbon-coated tungsten trioxide containing oxygen vacancies as photocatalysts for dye degradation, *J. Mater. Sci.* 54 (2019) 10656–10669, <https://doi.org/10.1007/s10853-019-03645-y>.
- [55] B.A. De Angelis, M. Schiavello, X-ray photoelectron spectroscopy study of nonstoichiometric tungsten oxides, *J. Solid State Chem.* 21 (1977) 67–72, [https://doi.org/10.1016/0022-4596\(77\)90145-1](https://doi.org/10.1016/0022-4596(77)90145-1).
- [56] Y. Li, Z. Tang, J. Zhang, Z. Zhang, Defect engineering of air-treated WO<sub>3</sub> and its enhanced visible-light-driven photocatalytic and electrochemical performance, *J. Phys. Chem. C* 120 (2016) 9750–9763, <https://doi.org/10.1021/acs.jpcc.6b00457>.
- [57] R. Chatten, A.V. Chadwick, A. Rougier, P.J.D. Lindan, The oxygen vacancy in crystal phases of WO<sub>3</sub>, *J. Phys. Chem. B* 109 (2005) 3146–3156, <https://doi.org/10.1021/jp045655r>.
- [58] S. Santucci, L. Lozzi, E. Maccallini, M. Passacantando, L. Ottaviano, C. Cantalini, Oxygen loss and recovering induced by ultrahigh vacuum and oxygen annealing on WO<sub>3</sub> thin film surfaces: influences on the gas response properties, *J. Vac. Sci. Technol.* 19 (2001) 1467–1473, <https://doi.org/10.1116/1.1349190>.
- [59] T.G.G. Maffei, D. Yung, L. LePennec, M.W. Penny, R.J. Cobley, E. Comini, G. Sberveglieri, S.P. Wilks, STM and XPS characterisation of vacuum annealed nanocrystalline WO<sub>3</sub> films, *Surf. Sci.* 601 (2007) 4953–4957, <https://doi.org/10.1016/j.susc.2007.08.009>.
- [60] Y.K. Park, C.J. Lim, Y.J. Im, S. Cho, S.W. Cho, H. Lee, H. Ogasawara, Soft X-ray spectroscopic study on the electronic structure of WO<sub>3</sub> thin films fabricated under various annealing temperature and gas flow conditions, *Curr. Appl. Phys.* 21 (2021) 31–35, <https://doi.org/10.1016/j.cap.2020.10.006>.
- [61] L. Sharma, P. Kumar, A. Halder, Phase and vacancy modulation in tungsten oxide: electrochemical hydrogen evolution, *ChemElectroChem* 6 (2019) 3420–3428, <https://doi.org/10.1002/celec.201900666>.
- [62] H. Yu, J. Guo, C. Wang, J. Zhang, J. Liu, G. Dong, X. Zhong, X. Diao, Essential role of oxygen vacancy in electrochromic performance and stability for WO<sub>3</sub>-y films induced by atmosphere annealing, *Electrochim. Acta* 332 (2020), 135504, <https://doi.org/10.1016/j.electacta.2019.135504>.
- [63] S. Rahimnejad, J.H. He, W. Chen, K. Wu, G.Q. Xu, Tuning the electronic and structural properties of WO<sub>3</sub> nanocrystals by varying transition metal tungstate precursors, *RSC Adv.* 4 (2014) 62423–62429, <https://doi.org/10.1039/c4ra10650d>.
- [64] T. Hussain, M.F. Al-Kuhaili, S.M.A. Durrani, A. Qurashi, H.A. Qayyum, Enhancement in the solar light harvesting ability of tungsten oxide thin films by annealing in vacuum and hydrogen, *Int. J. Hydrogen Energy* 42 (2017) 28755–28765, <https://doi.org/10.1016/j.ijhydene.2017.09.130>.
- [65] M. Vasilopoulou, I. Kostis, N. Vourdas, G. Papadimitropoulos, A. Douvas, N. Boukos, S. Kennou, D. Davazoglou, Influence of the oxygen substoichiometry and of the hydrogen incorporation on the electronic band structure of amorphous tungsten oxide films, *J. Phys. Chem. C* 118 (2014) 12632–12641, <https://doi.org/10.1021/jp502092h>.
- [66] A. Mozalev, M. Bendova, F. Gispert-Guirado, Z. Pytlíček, E. Llobet, Metal-substrate-supported tungsten-oxide nanoarrays via porous-alumina-assisted anodization: from nanocolumns to nanocapsules and nanotubes, *J. Mater. Chem. A* 4 (2016) 8219–8232, <https://doi.org/10.1039/c6ta02027e>.
- [67] A.H. Jayatissa, S.-T. Cheng, T. Gupta, Annealing effect on the formation of nanocrystals in thermally evaporated tungsten oxide thin films, *Mater. Sci. Eng., B* 109 (2004) 269–275, <https://doi.org/10.1016/j.mseb.2003.10.080>.
- [68] J.M. Berak, M.J. Sienko, Effect of oxygen-deficiency on electrical transport properties of tungsten trioxide crystals, *J. Solid State Chem.* 2 (1970) 109–133, [https://doi.org/10.1016/0022-4596\(70\)90040-X](https://doi.org/10.1016/0022-4596(70)90040-X).
- [69] J. Tauc, A. Menth, D.L. Wood, Optical and magnetic investigations of the localized states in semiconducting glasses, *Phys. Rev. Lett.* 25 (1970) 749–752, <https://doi.org/10.1103/PhysRevLett.25.749>.
- [70] E.A. Davis, N.F. Mott, Conduction in non-crystalline systems V. Conductivity, optical absorption and photoconductivity in amorphous semiconductors, *Philos. Mag. A J. Theor. Exp. Appl. Phys.* 22 (1970) 903–922, <https://doi.org/10.1080/14786437008221061>.
- [71] F. Wang, C. Di Valentin, G. Pacchioni, Electronic and structural properties of WO<sub>3</sub>: a systematic hybrid DFT study, *J. Phys. Chem. C* 115 (2011) 8345–8353, <https://doi.org/10.1021/jp201057m>.
- [72] M.B. Johansson, G. Baldissera, I. Valyukh, C. Persson, H. Arwin, G.A. Niklasson, L. Österlund, Electronic and optical properties of nanocrystalline WO<sub>3</sub> thin films studied by optical spectroscopy and density functional calculations, *J. Phys. Condens. Matter* 25 (2013) 1–11, <https://doi.org/10.1088/0953-8984/25/20/205502>.
- [73] P.P. González-Borrero, F. Sato, A.N. Medina, M.L. Baesso, A.C. Bento, G. Baldissera, C. Persson, G.A. Niklasson, C.G. Granqvist, A. Ferreira Da Silva, Optical band-gap determination of nanostructured WO<sub>3</sub> film, *Appl. Phys. Lett.* 96 (2010), 061909, <https://doi.org/10.1063/1.3313945>.
- [74] A. Rougier, F. Portemer, A. Quédé, M. El Marssi, Characterization of pulsed laser deposited WO<sub>3</sub> thin films for electrochromic devices, *Appl. Surf. Sci.* 153 (1999) 1–9, [https://doi.org/10.1016/S0169-4332\(99\)00335-9](https://doi.org/10.1016/S0169-4332(99)00335-9).
- [75] F. Zhang, H.Q. Wang, S. Wang, J.Y. Wang, Z.C. Zhong, Y. Jin, Structures and optical properties of tungsten oxide thin films deposited by magnetron sputtering of WO<sub>3</sub> bulk: effects of annealing temperatures, *Chin. Phys. B* 23 (2014), 098105, <https://doi.org/10.1088/1674-1056/23/9/098105>.
- [76] A. Subrahmanyam, A. Karuppasamy, Optical and electrochromic properties of oxygen sputtered tungsten oxide (WO<sub>3</sub>) thin films, *Sol. Energy Mater. Sol. Cells* 91 (2007) 266–274, <https://doi.org/10.1016/j.solmat.2006.09.005>.
- [77] J.B. Coulter, D.P. Birnie, Assessing Tauc plot slope quantification: ZnO thin films as a model system, *Phys. Status Solidi Basic Res.* 255 (2018) 1–7, <https://doi.org/10.1002/psb.201700393>.
- [78] N. Nagy, A. Deák, Z. Hörvölgyi, M. Fried, A. Agod, I. Bárony, Ellipsometry of silica nanoparticulate Langmuir - blodgett films for the verification of the validity of effective medium approximations, *Langmuir* 22 (2006) 8416–8423, <https://doi.org/10.1021/la061259j>.
- [79] G.E. Jellison Jr., V.I. Merkulov, A.A. Puzosky, D.B. Geohegan, G. Eres, D. H. Lowndes, J.B. Caughman, Characterization of thin-film amorphous semiconductors using spectroscopic ellipsometry, *Thin Solid Films* (2000) 377–378, [https://doi.org/10.1016/S0040-6090\(00\)01384-5](https://doi.org/10.1016/S0040-6090(00)01384-5), 68–73.
- [80] G.E. Jellison Jr., F.A. Modine, Parameterization of the optical functions of amorphous materials in the interband region, *Appl. Phys. Lett.* 69 (1996) 371–373, <https://doi.org/10.1063/1.118064>.
- [81] L. Valerio, K.-E. Peiponen, J.J. Saarinen, E.M. Vartiainen, *Kramers-Kronig Relations in Optical Materials Research*, first ed., Springer-Verlag Berlin Heidelberg, 2005 <https://doi.org/10.1007/b138913>.
- [82] R.A. Synowicki, Spectroscopic ellipsometry characterization of indium tin oxide film microstructure and optical constants, *Thin Solid Films* 313 (1998) 394–397, [https://doi.org/10.1016/S0040-6090\(97\)00853-5](https://doi.org/10.1016/S0040-6090(97)00853-5).
- [83] D.J. Dunstan, Evidence for a common origin of the Urbach tails in amorphous and crystalline semiconductors, *J. Phys. C Solid State Phys.* 15 (1982) L419–L424, <https://doi.org/10.1088/0022-3719/15/13/008>.
- [84] Y. Xin, H. Zhou, X. Ni, Y. Pan, X. Zhang, J.Y. Zheng, S. Bao, P. Jin, The optical properties of low infrared transmittance WO<sub>3</sub>-x nanocrystal thin films prepared by DC magnetron sputtering under different oxygen ratios, *RSC Adv.* 5 (2015) 57757–57763, <https://doi.org/10.1039/c5ra09518b>.
- [85] K. von Rottkay, M. Rubin, S.J. Wen, Optical indices of electrochromic tungsten oxide, *Thin Solid Films* 306 (1997) 10–16, [https://doi.org/10.1016/S0040-6090\(97\)00254-X](https://doi.org/10.1016/S0040-6090(97)00254-X).
- [86] M. Born, E. Wolf, *Principles of Optics*, seventh ed., Cambridge University Press, 2019 <https://doi.org/10.1017/CBO9781139644181>.
- [87] S. Sawada, G.C. Danielson, Optical indices of refraction of WO<sub>3</sub>, *Phys. Rev.* 113 (1959) 1008–1013, <https://doi.org/10.1103/PhysRev.113.1008>.
- [88] B.D. Viezicke, S. Patel, B.E. Davis, D.P. Birnie, Evaluation of the Tauc method for optical absorption edge determination ZnO thin films as a model system, *Phys. Status Solidi B* 252 (2015) 1700–1710, <https://doi.org/10.1002/psb.201552007>.